Temperature-dependent frictional properties of heterogeneous Hikurangi Subduction Zone input sediments, ODP Site 1124

Carolyn Boulton[1], André R. Niemeijer[2], Christopher J. Hollis[3], John Townend[1], Mark D. Raven[4], Denise K. Kulhanek[5], Claire L. Shepherd[3]

[1]School of Geography, Environment, and Earth Sciences, Victoria University of Wellington, Wellington, New Zealand
[2] Faculty of Geosciences, HPT Laboratory, Utrecht University, Utrecht, the Netherlands
[3]GNS Science, Lower Hutt, New Zealand
[4]CSIRO Land and Water/Mineral Resources, Urrbrae, South Australia
[5]IODP, Texas A&M University, College Station, Texas, USA
corresponding author: Carolyn Boulton (carolyn.boulton@vuw.ac.nz)

Key Points:

- Frictionally weak Eocene clays occur between Paleocene and Oligocene chalks
- With increasing temperature, (*a*–*b*) increases in clays and decreases in chalks
- Subduction zone input sediments exhibit heterogeneous frictional strength and stability properties

Abstract

The Hikurangi Subduction Zone (HSZ), New Zealand, accommodates westward subduction of the Pacific Plate. Where imaged seismically, Late Cretaceous-Paleogene (70–32 million-year-old) sediments host the shallow HSZ décollement (<10–15 km depth). The frictional properties of Paleogene sediments recovered from Ocean Drilling Program Leg 181, Site 1124 were measured at 60 MPa effective normal stress and varying sliding velocities (V=0.3–30 μm/s) and temperatures (T=25–225°C). Velocity-stepping experiments were conducted at temperatures of 25°C, 75°C, 150°C, and 225°C to determine the friction rate parameter (a–b). Paleocene and Oligocene clay-bearing nannofossil chalks (μ=0.45–0.61) and a middle Eocene clayey nannofossil chalk (μ=0.35–0.51) are frictionally stronger than smectite-bearing Eocene clays (μ=0.16–0.31). With increasing temperature, chalks show rate-strengthening to rate-weakening frictional stability trends; clays show rate-neutral to rate-strengthening trends. The results obtained from Site 1124 sediments indicate that: (1) fault-zone weakness may not require pore-fluid overpressures; (2) clays and chalks can host frictional instabilities; and (3) heterogeneous frictional properties can promote variable slip behaviour.

Keywords: *friction, stability, mineralogy, subduction zone, creep, seismicity*

1. Introduction

Subduction zones are formed where one tectonic plate plunges beneath another and are responsible for the largest earthquakes and tsunamis on Earth. However, slip on subduction zone faults is not always seismic: failure modes also include aseismic creep, slow slip events, low-frequency earthquakes, and tremor (e.g., Schwartz and Rokowsky, 2007; Peng and Gomberg, 2010; Bartlow et al., 2011; Avouac, 2015). The North Island of New Zealand overlies the Hikurangi Subduction Zone (HSZ), which accommodates westward subduction of the Pacific plate at rates that decrease southwards from ~60 to ~20 mm yr^{-1} (Fig. 1) (Wallace et al., 2004, 2009). Geodetic and seismological data have revealed profound spatial variations in the HSZ's seismic behaviour and provide evidence for a complex interplay between seismic earthquakes and aseismic creep: that is, between fast and slow slip on the plate boundary (e.g., Douglas et al., 2005; Wallace et al., 2004, 2009, 2012, 2017; Eberhart-Phillips and Bannister, 2015; Todd and Schwartz, 2016).

Along the northern HSZ margin, the décollement experiences shallow (< 15 km depth), short duration (usually 2–3 weeks) slow slip events (SSEs) which recur every 1–2 years (Fig. 1); there, the transition to aseismic creep occurs at 10-15 km depth (Douglas et al., 2005; Delahaye et al., 2009; Wallace et al., 2009, 2017; Lamb and Smith, 2013). Offshore Gisborne, the region coincident with slow slip has also ruptured historically in large-magnitude tsunamigenic earthquakes in March (M_w 7.0-7.1) and May (M_w 6.9-7.1) 1947 (Doser and Webb, 2003). Along the southern HSZ margin, long-duration (1–2 years) SSEs occur at 30-70 km depth every 5–10 years, and the up-dip décollement is fully locked (Wallace et al., 2009, 2012; Lamb and Smith, 2013) (Fig. 1). Although there are no historical records of earthquakes larger than magnitude M_w 6.5 on the locked fault, paleoseismic evidence suggests that the plate interface periodically hosts large to great tsunamigenic events (Clark et al., 2015).

Beneath the North Island, the subducting plate comprises the Hikurangi Plateau, thick, buoyant basaltic crust overlain by up to ~4 km of Cretaceous volcaniclastics and Paleogene to Neogene marine sediments (Davy et al., 2008; Bell et al., 2010). The northern HSZ margin offshore Gisborne has an over-steepened frontal slope and is underlain by numerous seamounts, creating a rough subduction zone interface (Barker et al., 2009; Pedley et al., 2010). In contrast, a broad accretionary wedge replete with well-developed splay faults overlies the décollement along the southern HSZ margin (Barnes et al., 2010; Bassett et al., 2014; Ghisetti et al., 2016). The transition between the two morphologies occurs gradually between Napier and Cape Turnagain and is accompanied by an along-strike decrease in the angle between the direction of plate convergence and the Hikurangi Trough, from almost orthogonal in the north to an oblique angle of ~40° in the south (Wallace et al., 2009). Overall, the change in slip mode observed from north-to-south on the shallow HSZ décollement may reflect changes in: (1) the composition and thickness of subducting marine sediments, (2) plate geometry, including dip and fault roughness, (3) effective normal stress, and/or (4) decreasing plate convergence rate (e.g., Barker et al., 2009; Fagereng and Ellis, 2009; Wallace et al., 2009; Fagereng, 2011a; Gao and Wang, 2014; Eberhart-Phillips and Bannister, 2015; Heise et al., 2017; Skarbek and Rempel, 2017). Within this context, we document variations in marine sediment composition, strength, and stability at one downgoing plate locality.

Depth-migrated, geologically interpreted seismic lines indicate that the shallow HSZ décollement (<~15 km depth) occurs in Upper Cretaceous-Paleogene (70–32 million-year-old) marine sediments (Plaza-Faverola et al., 2012, 2016; Ghisetti et al., 2016). The HSZ décollement progressively steps down to volcaniclastic units comprising the top of the Hikurangi Plateau at greater depths (Plaza-Faverola et al., 2016), but this research focuses on the shallow décollement, which exhibits along-strike variations in interseismic coupling (e.g., Delahaye et al., 2006; Wallace et al., 2004, 2009; Bell et al., 2010) (Fig. 1). At the time of this research, the only Hikurangi Plateau Cretaceous-Pleistocene cover sequence samples available for friction experiments were collected during the Ocean Drilling Program (ODP) Leg 181 at Site 1124 (39.4984°S, 176.5316°E), located at 3978 m water depth approximately 400 km east of the Hikurangi Trough (Fig. 1, 2) (Carter et al., 1999, 2004).

Paleogene sedimentation at Site 1124 is pelagic, similar to the input sequence recently cored during IODP Expedition 375 at trench-proximal Site U1520 (38.9692°S, 179.1318°E), located at 3522 m water depth (Fig. 1, 2) (Carter et al., 1999; Saffer et al., 2018). Within the Site 1124 pelagic sequence, shipboard data collected from Hole 1124C identified a clay-rich ("dark mudstone") interval at 425 m below the sea floor (mbsf) bounded by calcareous sediments; geophysically, the clay-rich interval is characterized by high magnetic susceptibility and natural gamma, low density, high porosity, and high water contents (Carter et al., 1999, 2004). Here, we present biostratigraphic and mineralogical data from nine samples spanning the Hole 1124C clay-rich interval, report the results of hydrothermal friction experiments performed on each sample, and discuss how sediment composition can influence subduction zone seismic style.

2. Age and mineralogy

2.1 Analytical methods

Nine samples were taken from core recovered between 419.10 mbsf and 434.56 mbsf in ODP Hole 1124C. Samples are labelled herein following ODP convention, whereby the leg, hole, core, and section are separated by hyphens, followed by centimeters below the top of the section (Fig. 2, 3). Splits were prepared for calcareous nannofossil analysis and quantitative X-ray diffraction (XRD). Nannofossil analyses were performed on standard smear slides (Bown and Young, 1998) at 1000× magnification under cross-polarized and plane-transmitted light. At least two traverses of a 40 mm coverglass were examined to document the assemblage. Nannofossil results are correlated to the NP zones of Martini (1971) (Appendix Table A.1). XRD analyses were performed on micronized, calcium-saturated random powders with a PANalytical X'Pert Pro Multi-Purpose Diffractometer using Fe-filtered Co Kα radiation and a fast X'Celerator Si strip detector. Diffraction patterns recorded from 3° to 80° in steps of 0.017°2θ were analysed quantitatively using the commercial software SIROQUANT (Fig. A.1).

2.2 Results

The calcareous nannofossil biostratigraphy of the Paleocene–Eocene transition in ODP Hole 1124C is complicated by an unconformity between cores 45X and 44X and pervasive sediment mixing in the lower part of core 44X (Fig. 3, 4). The interval from the base of core 46X (445.54 mbsf) to sample 181-1124C-45X-1, 17-21 cm (429.17 mbsf) is correlated to early Paleocene nannofossil Zones NP4 and NP5 (Appendix Table A.1) based on the presence of *Chiasmolithus bidens*, *Sphenolithus primus*, and *Fasciculithus tympaniformis*, and the absence of any *Heliolithus* or *Discoaster* species. Samples from the core catcher (CC) of core 44X (428.90–428.75 mbsf) contain a mixture of earliest late (hereafter mid-) Paleocene and middle Eocene species, indicating that either Paleocene species have been reworked into younger sediments or that bioturbation has mixed Eocene species into older sediments. The overlying sample 181-1124C-44X-7, 4-6 cm (428.34 mbsf) is barren of nannofossils, but the interval above (427.3–424.3 mbsf) is correlated with middle Eocene nannofossil Zone NP16 based on the persistent occurrence of *Reticulifenestra umbilicus*. Shipboard studies indicate a hiatus at ~419.3 mbsf between the middle Eocene and lower Oligocene (Fig. 4) (Carter et al., 1999).

Mineralogically, the oldest mid-Paleocene and youngest early Oligocene samples contain 66 to 83% calcite and minor amounts of smectite (montmorillonite), quartz, plagioclase, mica, and zeolite. Mid-Paleocene to middle Eocene samples containing 45–57% montmorillonite and 12–24% zeolite form an approximately 3 m-thick interval (Table 1) (Fig. 4). The zeolite is a mixture of heulandite and clinoptilolite (Carter et al., 1999; this study) (Appendix Table A.2) (Fig. A.1). The sediments are named following Dean et al. (1985). Samples 181-1124C-43X-CC; 44X-CC (light-colored lithology); 45X-2, 78-82 cm; and 45X-5, 53-56 cm are firm, clay-bearing nannofossil chalk (abbreviated chalk). Sample 44X-4, 50-53 cm is a firm, clayey nannofossil chalk (abbreviated clayey chalk). Samples 44X-5, 50-53 cm; 44X-6, 50-53 cm; 44X-CC (dark-colored lithology) are nannofossil-bearing clays, and 44X-7, 4-6 cm is a clay (abbreviated clay). The term “clay” is used to describe sediment containing >50% clay minerals (Dean et al., 1985).

3. Frictional properties

3.1 Experimental methods

Samples were disaggregated and milled for five minutes in a McCrone mill, producing starting materials with a grain size of less than 10 μm (Fig. A.2). All hydrothermal friction experiments were performed in a ring shear apparatus following Niemeijer et al. (2008) and den Hartog et al. (2012a) (Appendix Fig. A.3). During each experiment, a pre-pressed ring-shaped gouge sample with an initial thickness of 1.0–1.4 mm was placed between two pistons, loaded, and allowed to consolidate for approximately 30 minutes. Deformation occurred in an internally heated pressure vessel at an effective normal stress (σ_n') of 60 MPa

(100 MPa total applied load, less 40 MPa pore pressure (P_p), equivalent to a pore fluid factor, $\lambda = P_p/\sigma_v$, of 0.4). Effective normal stress conditions are equivalent to approximately 4 km depth on the décollement assuming an overburden density of 2500 kg/m^3 and hydrostatic pore fluid pressure.

A servo-controlled electromotor sheared the gouge at a velocity (V) of 1 μm/s for 1.5 mm to achieve a steady-state coefficient of friction (μ), defined as shear stress divided by effective normal stress ($\mu = \tau/\sigma_n'$) ignoring cohesion. Velocity stepping tests from 0.3–30 μm/s were then performed to determine the friction rate parameter (*a–b*). Approximately 17 mm of displacement occurred during each experiment, and frictional properties were measured at temperatures of 25, 75, 150, and 225°C. The friction rate parameter (*a–b*) was quantified using an iterative least-squares method incorporating the Dieterich (1979) rate-and-state friction equation:

$$\mu = \mu_0 + a\ln\left(\frac{V}{V_0}\right) + b_i\ln\left(\frac{V_0\theta_i}{D_{c_i}}\right), \text{ with } \frac{d\theta_i}{\mathrm{d}t} = 1 - \frac{V\theta_i}{D_{c_i}} \quad (1)$$

Here, μ is the instantaneous friction coefficient, μ_0 is a reference friction coefficient at velocity V_0, θ is a state variable, *a* and *b* are constants, and D_c is the critical slip distance (Saffer and Marone, 2003) (Appendix Table A.3-A.6). The subscripts for *b*, θ, and D_c represent separate evolution processes. At steady-state, the friction rate parameter (*a–b*) is defined in terms of the logarithmic velocity-dependence of friction following:

$$(a - b) = \frac{\partial \mu_{ss}}{\partial \ln V} \quad (2)$$

Positive values of (*a–b*) indicate that a material is intrinsically stable and rate-strengthening. A material with negative (*a–b*) values is rate-weakening and can nucleate a frictional instability if fault stiffness (*k*) is less than a critical stiffness (k_c):

$$k_c = \frac{-(a-b)\sigma_n'}{D_c} \quad (3)$$

Slow slip events occur where (a–b) is negative, k is positive, and $k_c \approx k$ (e.g., Leeman et al., 2016) or, alternatively, where the spatial distribution of rate-weakening materials is insufficient to allow an instability to accelerate (Liu and Rice, 2007; Rubin, 2008; Skarbek et al., 2012). Following each experiment, sheared samples were impregnated with epoxy. Two samples were mounted on a scanning electron microscope (SEM) stub, broad-ion-beam polished using a Fischione model 1060 SEM mill polisher, and imaged using a FEI XL30S FEG SEM at the Utrecht University Electron Microscopy Square.

3.2 Experimental results

Frictional strength correlates strongly with the proportion of the clay mineral smectite. Clays containing smectite are frictionally weak (μ=0.16–0.31). Clay-bearing nannofossil chalks (chalks) and a clayey chalk above and below this interval contain more calcite (47–85%) and are frictionally stronger (μ=0.35–0.61) (Table 1) (Fig. 5, 6). Frictional stability also varies with mineralogical composition: with increasing temperature, values of (a–b) become more positive for clays (i.e., more rate-strengthening and prone to aseismic creep), and more negative for chalks (i.e., more rate-weakening and prone to seismic slip) (Fig. 7). The clayey chalk exhibits intermediate behaviour (Fig. 5, 6, 7). Importantly, at temperatures of 25°C and 75°C, the clays are rate-weakening to rate-neutral; the most clay-rich samples show rate-weakening behaviour at the lower temperatures (Table 1, Appendix Table A.3, A.5) (Fig. 7a). The chalks exhibit both rate-weakening and rate-strengthening behaviours at T=150°C, but they are rate-weakening at all velocities at T=225°C (Table 1, Appendix Table A.4, A.6) (Fig. 7d).

Changes in the friction rate parameters *a* and *b* as a function of temperature and velocity appear in Figures 8 and 9, respectively. Hole 1124C clays (52-57% montmorillonite; experiments u644, u713, u639) exhibit a positive correlation between sliding velocity and *a* and *b* (Fig. 9a, 9c). With increasing temperature, *a* increases (Fig. 8a) and *b* decreases (Fig. 8c). Increasing values of *a* and decreasing values of *b* result in the observed transition from rate-weakening (negative *a–b*) to rate-strengthening (positive *a–b*) behaviour with increasing temperature (Fig. 7a, 7c). Across the range of temperatures investigated, Hole 1124C chalks (66-85% calcite; experiments u643, u645, u657, and u656) exhibit no correlation between the friction rate parameters *a* and *b* and temperature or sliding velocity (Fig. 8b, 8d, 9b, 9d). Overall, (*a–b*) decreases in the chalks with increasing temperature (Fig. 7b, 7d). However, the individual rate parameters could not be measured because of stick slip instabilities during some velocity steps at *T*=150°C and all velocity steps at *T*=225°C (e.g., Fig. 5).

Microstructurally, fault-parallel B and Y shears, along with oblique R_1 and P shears, developed in a sheared chalk (u643, 181-1124C-43X-CC) (nomenclature of Logan et al., 1992) (Fig. 10a, 10c, 10e). The brittle B, Y, R_1 and P shears are characterized by cataclastic grain size reduction involving fragmentation, translation, and rotation (Fig. 10c). In contrast, a sheared clay (u644, 181-1124C-44X-7, 4-6 cm) accommodated slip by distributed sliding on an anastomosing foliation defined by discontinuous Y and P shears along which clay mineral foliae are aligned (Fig. 10b, 10d, 10f). Unbroken grains of quartz, plagioclase, and titanium oxide are completely encompassed by fine-grained clay minerals (Fig. 10d).

4. Discussion

4.1 Environmental and depositional context of the Paleogene clays

Site 1124 on the Hikurangi Plateau has remained at bathyal to upper abyssal depths throughout the Cenozoic (Fig. 1). During the mid-Paleocene to middle Eocene, pelagic sedimentation prevailed and smectite was deposited via differential settling from marine currents and eolian dust; minor amounts of authigenic smectite may have formed from the reaction of dissolved silica and iron hydroxides (Hillier, 1995; Kastner*,* 1981, 1999). Conditions also favoured authigenic zeolite formation (Table 1) (Kastner, 1999). During the Eocene, global climatic warming events such as the Paleocene-Eocene thermal maximum (PETM) (Nicolo et al., 2007; Slotnick et al., 2012), the early Eocene climatic optimum (EECO) (Hollis et al., 2005a, b; Slotnick et al., 2015), and the middle Eocene climatic optimum (MECO) (Hollis et al., 2005a) raised temperatures regionally (Bijl et al., 2009; Hollis et al., 2012) and promoted chemical weathering, terrigenous run-off (Crouch and Visscher*,* 2003), and smectite (± kaolinite) deposition (e.g, Thiry, 2000; Zachos et al., 2005). In Hole 1124C, mineralogical trends are consistent with enhanced smectite deposition during warm Eocene climatic events (Table 1) (Fig. 4). Smectite content increases in the lower part of core 44X, directly above the Paleocene/Eocene unconformity, and it decreases in the basal Oligocene (Fig. 2, 3, 4). The increase in smectite recorded at Site 1124 during the Eocene is widely observed from the northern East Coast Basin siliciclastic sediments (Field et al., 1997) to the southern East Coast Basin pelagic sequence (Slotnick et al., 2012, 2015; Hines et al., 2013) (Fig. 1).

4.2 Comparison of experimental results with previous studies

Site 1124 pelagic sediment strength and stability data can be compared with experimental results obtained from the end-member compositions, pure montmorillonite and pure calcite. At room temperature, clays with 52–57% montmorillonite are marginally stronger (average $\mu = 0.22$) and less stable (average $a–b = –0.0006$) than pure montmorillonite gouges tested under controlled pore-fluid pressure, drained conditions, and 20–100 MPa effective normal stress (average $\mu = 0.11–0.12$) (average $a–b$=0.0004–0.0005 for 0.1–1 μm/s v-step) (Tembe et al., 2010; Morrow et al., 2017). With increasing temperature, frictional strength generally increases in Site 1124 clays, and average values of (a–b) increase systematically from –0.0006 at 25°C to 0.0005 at 75°C, 0.002 at 150°C, and 0.005 at 225°C (Fig. 6, 7) (Appendix Table A.3, A.5).

Pure Na-montmorillonite gouges deformed at 50–70 MPa effective normal stress exhibited little variation in strength with temperature, with μ consistently 0.05–0.09, and underwent a transition from rate-weakening to rate-strengthening at T≥90°C (Mizutani et al., 2017). In addition, the hydrothermal frictional properties of hemipelagic clay (67% montmorillonite) recovered from the Japan Trench during Expedition 343 (JFAST) at Site C0019 were measured at 50 MPa effective normal stress (Chester et al., 2013; Sawai et al., 2017). The hemipelagic clay exhibited a temperature-dependent friction coefficient between 0.31 and 0.38. Like the Site 1124 clays, the JFAST clay transitioned from rate-weakening to rate-strengthening at T=150–200°C; repeat velocity steps showed that the transition was temperature, not strain, dependent (Sawai et al., 2017).

At room temperature, Site 1124 pelagic chalks (66–83 wt.% calcite) have a broad range of friction coefficients (μ = 0.45-0.62) and friction rate parameters (a–b = –0.0006–0.005) (Table 1) (Fig. 6, 7). Gouges composed of pure calcite (crushed Iceland spar) tested under controlled pore-fluid pressure, drained conditions, and 50 MPa effective normal stress have marginally higher friction coefficients (μ = 0.66–0.72) and rate-neutral to rate-strengthening behaviour (a–b = –0.0003–0.0096 for v-steps between 0.1 and 10 μm/s) (Verbene et al., 2014, 2015; Chen et al., 2015). Site 1124 chalks containing ≥66 wt.% calcite become increasingly unstable at higher temperatures and undergo stick-slip instabilities at 150°C and 225°C (Table 1) (Fig. 7b, 7d). Experiments on pure calcite also show increasingly negative values of (*a*–*b*) at temperatures exceeding 80°C (Verberne et al., 2014, 2015; Chen et al., 2015).

An Eocene clayey chalk with an intermediate composition (47% calcite and 38% phyllosilicates) shows similar frictional strength (μ=0.35–0.51; *T*=25–225°C) and stability (*a*–*b* = 0.006–0.003; *T*=25–225°C) properties to a Miocene clayey chalk (43% calcite and 20% phyllosilicates) recovered from Hole 1124C (Rabinowitz et al., 2018). The Miocene sample, amalgamated from core recovered between 194 mbsf and 213.48 mbsf (Fig. 2), exhibited friction coefficients between ~0.2 and ~0.5 across a range of applied normal stresses (σ_n=1–152 MPa). Neither the Eocene clayey chalk's nor the Miocene clayey chalk's frictional properties were temperature-dependent in the range *T*=20–100°C (Table 1) (Rabinowitz et al., 2018). Interestingly, the Miocene clayey chalk exhibited rate-neutral to rate-strengthening behaviour except at 10 MPa applied normal stress in two room-temperature, uncontrolled pore-fluid pressure experiments performed to simulate plate-convergence rates. During slow velocity steps between 0.017 μm/s and 0.51 μm/s, the clayey chalk was rate-weakening (Rabinowitz et al., 2018).

Following Tembe et al. (2010), we infer that the frictional properties of fault gouges are governed by the mineralogy of the load-bearing matrix. In polymineralic pelagic sediments containing predominantly smectite and carbonate, frictional weakness (μ<0.3) results when phyllosilicates (montmorillonite + white mica ± kaolin) comprise more than 50% of the sediment (Fig. 4, 6). A clayey chalk and chalks containing 10–38% phyllosilicates are frictionally stronger at every temperature tested in the hydrothermal friction experiments; we infer that granular calcite contacts influenced the strength and stability of the clayey chalk and chalks (Table 1, Appendix Table A.2) (Fig. 5, 6, 7). These results are consistent with those of Tembe et al. (2010), who found that montmorillonite and illite contents greater that

40-50% were required to isolate grains of frictionally stronger minerals, such as quartz and calcite. Frictional weakness may occur with lower proportions of phyllosilicates (<40%) if those present are aligned and form an interconnected foliation along which localized sliding occurs (e.g., Collettini et al., 2009; Tesei et al., 2014). As little as 20% of the weak phyllosilicate talc, common in altered ultramafic rocks, may reduce the friction coefficient of calcite-talc gouges to $\mu<0.4$ (Giorgetti et al., 2015).

4.3 Interpretation of changes in the friction rate parameters

The mineralogy of the load-bearing matrix also governs the evolution of frictional contacts following changes in velocity, temperature, and/or displacement (e.g., Blanpied et al. 1995, 1998; Bos and Spiers, 2002; Morrow et al., 2017). The empirically derived rate and state (R-S) friction equations (Equations 1 and 2) describe the velocity-dependent change in friction that results from changes in frictional contact area and changes in the strain-rate dependent strength of contacts (e.g., Dieterich, 1979; Ruina, 1983; Nakatani, 2001). However, identifying the microphysical processes underpinning the R-S friction equations remains an outstanding research topic (e.g., Chen et al., 2017 and references therein). To understand the trends in (a–b) exhibited by the Hole 1124C clays and chalks, the friction rate parameters a and b (the sum of b_1 and b_2 where two state variables were required to fit a velocity step), and the critical slip distance(s) D_c were plotted as a function of velocity and temperature (Fig. 8, 9) (Appendix Fig. A.4, A.5, A.6, and A.7).

As temperature increases from 25°C to 225°C in the Hole 1124C clays (52-57% montmorillonite; experiments u644, u713, u639), the direct effect, $a=a \ln (V/V_0)$, exhibits small increases in median and mean values, a trend also observed with increasing velocity (Fig. 8, 9). At the same time, the total evolution effect, $b= b \ln (V_0\theta/D_c)$, shows no correlation with velocity and decreases with increasing temperature, with the mean and median values of *b* becoming negative at T=225°C (Fig. 8, 9). The critical slip distance(s) D_c do not show any correlation with velocity or temperature. Increasing values of *a* and decreasing values of *b*, to near-zero at T≥150°C, result in the observed transition from rate-weakening (negative *a*–*b*) to rate-strengthening (positive *a*–*b*) behaviour with increasing temperature in the montmorillonite-rich clays (Fig. 7a, 7b, 8, 9).

The evolution effect is usually interpreted to result from a change in the total contact area following a change in velocity (e.g., Marone, 1998). Positive values of *b* reflect a transient decrease in contact area with an instantaneous increase in velocity, and thus a transient decrease in the coefficient of friction (e.g., Sammis and Steacy, 1994; Niemeijer and Spiers, 2006; Chen et al., 2017). A common explanation for the near-zero values of *b* commonly observed in clay-rich gouges is that the sheet-like clays align during sliding, maximizing the available contact area. When contact area is saturated, there is little potential for contact area change following a velocity step, and vanishingly small *b* values occur (Saffer and Marone, 2003; Ikari et al., 2009; Smith and Faulkner, 2010; see also Morrow et al., 2017). In partially drained or undrained conditions, where pore-fluid overpressures have developed, negative *b* values may result from a decrease in pore-fluid pressure concomitant with dilation upon an increase in sliding velocity (e.g., Samuelson et al., 2009; Faulkner et al., 2018). However, we intentionally sheared our thin (<1 mm-thick) gouge layers at low sliding velocities to avoid pore-fluid overpressure development. To provide a definitive microphysical explanation for the observed trends, a detailed understanding of the composition and geometry of frictional contacts in fluid-saturated montmorillonite-bearing gouges at varying temperatures, pressures, and strain rates is required (e.g., Moore and Lockner, 2004; Behnsen and Faulkner, 2013; Sakuma and Suehara, 2015; Sanchez-Roa et al., 2017; Morrow et al., 2017).

For the chalks (66-85% calcite; experiments u643, u645, u657, and u656), the individual rate parameters *a* and *b*, along with the critical slip distance(s) *Dc*, show no discernible trend with increasing velocity or temperature (Fig. 8, 9). However, the 1-0.3 μm/s, 0.3-1 μm/s, and 1-3 μm/s velocity steps at *T*=150°C, and all velocity steps at *T*=225°C, resulted in stick-slip events, and it was not possible to obtain accurate values for the individual parameters from those steps. Nevertheless, the appearance of stick-slip events at *T*=150°C suggests that *b* values became larger at this temperature, resulting in net negative values of (*a*–*b*).

A (positive) increase in the evolution effect, *b*, at lower sliding velocities and higher temperatures might be explained by enhanced compaction in saturated granular gouges comprising soluble minerals such as calcite (Zhang et al., 2010; Chen and Spiers, 2016). For a given velocity, time-dependent, fluid-assisted compaction (i.e., pressure solution) leads to a lower steady state porosity and larger increase in contact area. At a higher velocity, compaction processes operate less efficiently, resulting in a higher porosity, smaller contact area, and lower friction coefficient (e.g., Niemeijer and Spiers, 2006; Chen and Spiers, 2016; Chen et al., 2017). In previous experiments on carbonates, it was suggested that fluid-assisted compaction decreases porosity, increases contact area, increases *b* values, and drives the transition from rate-strengthening to rate-weakening behaviour (Verberne et al., 2014; Pluymakers et al., 2014; Chen and Spiers, 2016). We propose that at *T*≥150°C, time-dependent fluid-assisted compaction operated in our experiments as well.

4.4 Application of experimental results to megathrust strength and stability

In the context of a single-degree-of-freedom spring-block slider, the criterion for unstable fault behaviour is defined by the interaction between the rheological stiffness of the fault, k_c, and the loading system stiffness, k (Equation 3) (Gu et al., 1984; Leeman et al., 2016). Negative values of (*a*–*b*), as observed in chalks at T≥150°C leads to higher critical stiffness values, making earthquake nucleation easier. Positive values of (a–b), as observed in clays at T≥150°C and chalks at T≤150°C, result in negative critical stiffness, inhibiting the nucleation of seismic slip and promoting aseismic creep. Slow slip occurs near the transition between unstable and stable behaviour, where $k \approx k_c$. This condition is favoured by near-neutral values of (a–b), low effective normal stress, and/or a large critical slip distance (D_c) (Liu and Rice, 2007; Rubin, 2008; Saffer and Wallace, 2015; Wei et al., 2018). Frictionally weak clays recovered at Site 1124 exhibit negative to near-neutral values of (a–b) at temperatures between 25°C and 75°C (Fig. 6a). Accelerating slip can develop into a seismic instability depending on the spatial distribution of the clays and the slip-dependent activation of any arresting mechanisms such as dilatant strengthening or accelerating mechanisms, such as pore-fluid pressurization (e.g., Liu and Rice, 2007; Segall et al., 2010; Samuelson et al., 2010; Faulkner et al., 2011, 2018) (Table 1). Within fault zones, pore fluid pressure is expected to vary spatiotemporally because of time-, temperature-, velocity- and displacement-dependent changes in porosity, permeability, and fluid flux (e.g., Segall et al., 2010; Kitajima and Saffer, 2012; Ellis et al., 2015; Faulkner et al., 2011, 2018).

Fault slip mode may also be controlled by the relative distribution of rate-weakening and rate-strengthening sediments, both of which occur within the Paleogene sequence of sediments cored at Site 1124 (Fagereng, 2011b; Skarbek et al., 2012). Studies of exhumed and cored subduction zone faults indicate that at depths exceeding 1–2 km, multiple, anastomosing slip surfaces form a décollement ~100–350 m thick (Rowe et al., 2013). Within a wide décollement, slip along multiple surfaces would juxtapose clays and chalks, repeat stratigraphic units, and create a mélange composed of frictionally strong chalk clasts in a matrix of weak clays (e.g., Fagereng and Sibson, 2010). Numerical rate-and-state friction simulations of fault zones with heterogeneous distributions of rate-weakening and rate-strengthening materials and effective normal stresses reproduce the full spectrum of fault slip behaviour (Skarbek et al., 2012; Luo and Ampuero, 2017). Such simulations, which represent the fault as a series of spring-block sliders with two degrees of freedom, suggest that slip mode is controlled primarily by the relative strength ratio (α) of rate-weakening (subscript *w*) and rate-strengthening (subscript *s*) materials,

$$\alpha = \frac{(b_w - a_w)\sigma'_w}{(a_s - b_s)\sigma'_s} \tag{4}$$

where a and b are the friction rate parameters and σ' is the effective normal stress acting on each material (Luo and Ampuero, 2017). Slip mode also depends on the critical length of the rate-weakening component, which scales with the shear modulus divided by the critical stiffness k_c (Equation 3) (Luo and Ampuero, 2017; McLaskey and Yamashita, 2017). In our experiments, the relative strength ratio is low at temperatures between 25°C and 75°C because clays and chalks exhibit small negative and small positive (*a–b*) values, respectively (Fig. 7a, 7b, 11a). A low relative strength ratio promotes aseismic creep and slow slip (Fig. 11). Between 150°C and 225°C, the relative strength ratio increases due to larger negative (*a–b*) values for chalks (Fig. 7c, 7d, 11a); an increase in α would encourage seismic slip given an adequate distribution of rate-weakening material(s) (Equation 4).

Microstructures examined here resulted from deformation across a range of velocities (0.3 – 30 μm/s) at progressively higher temperatures and strains (Fig. 5, 10). Additional experiments at constant temperature, velocity, and strain would be required to thoroughly investigate the effect these parameters have on microstructural development (e.g., Logan et al., 1992; Bos and Spiers, 2001). In the experiments performed, deformation is distributed in a clay (44X-7, 4-6 cm) sheared at temperatures up to 225°C, conditions at which it exhibits positive values of (*a–b*) (Fig. 7c, 10b). Distributed deformation, combined with rate-strengthening behaviour, promotes widening of the décollement and enables sediment mixing to take place, particularly within poorly lithified sediments (e.g., Maltman, 1994;

Mittempergher et al., 2018). Wide mélange zones containing competent clasts embedded in clay-rich matrices are a characteristic of subduction zone megathrusts developed at all levels within the brittle crust (e.g., Cloos and Shreve, 1988; Kimura et al., 2012; Fagereng, 2013; Rowe et al., 2013).

In contrast, deformation localizes in a sheared chalk (43X-CC, light-coloured lithology), which exhibits negative values of (*a*–*b*) at temperatures at and above 150°C (Fig. 7d, 10a) (e.g., Verbene et al., 2014, 2015). Deformation localization in frictionally strong, rate-weakening chalks would promote earthquake nucleation and propagation along discrete slip surfaces (e.g., Tesei et al., 2014; Verberne et al., 2014, 2015; Gratier et al., 2013; Bullock et al., 2015). The laboratory friction experiments were performed on 1 mm-thick simulated gouge layers. However, field observations of a large-displacement fault zone developed in Middle to Late Eocene southern East Coast Basin calcareous clays and marls demonstrate the propensity for these units to form tectonic mélanges (Fig. 1, 11b) (Hungaroa Fault Zone, Hines et al., 2013). Our experimental, microstructural, and field observations indicate that quantifying the on-fault distribution of rate-strengthening and rate-weakening materials may be key to understanding slip behaviour that ranges from distributed, aseismic creep to localized seismic-wave-radiating earthquake ruptures (Fig. 11b) (Fagereng and Sibson, 2010; Fagereng, 2011b; Skarbek et al., 2012; Avouac, 2015; Luo and Ampuero, 2017).

Globally, the brown clays and carbonates studied herein comprise between ~7% and ~10%, respectively, of all subducting sediments (Plank and Langmuir, 1998; Plank, 2014). Summarizing results from 26 Ocean Drilling Program (ODP) and Deep Sea Drilling Project (DSDP) drill sites, Plank (2014) documented calcareous and brown clay sediments occurring together in core recovered from the Hikurangi (ODP Site 1124), Kermadec (ODP Site 1124, DSDP Sites 595 and 596), Vanuatu (DSDP Site 286), East Sunda (DSDP Site 261 and ODP Site 765), Philippine (DSDP Site 291), Marianas (ODP Site 800), Izu-Bonin (ODP Site

1149), Honshu (DSDP Sites 303 and 304), and Peru (DSDP Site 321) trenches. Carbonates occur alone in the Columbia (DSDP Site 505 and ODP Site 677) trench, with siliceous sediments in the Guatamala (DSDP Site 495) trench, and with siliceous sediments and gabbro in the Costa Rica (ODP Sites 1039 and 1253) trench. Brown clays occur alone or with siliceous sediments in the Tonga (DSDP Sites 595 and 596), Marianas (ODP Site 801), Alaska (DSDP Site 178), Mexico (DSDP Site 487), Northern and Central Chile (ODP Site 1232), Sandwich (ODP Site 701), and Northern Antilles (DSDP Site 543) trenches (Plank, 2014 and references therein).

4.5 Pore-fluid overpressure development and its mechanical implications

Seismic-reflection data have been interpreted to indicate the presence of high-pressure fluids within northern HSZ décollement sediments that experience slow slip events at depths between <5 km and >10–16 km (Bell et al., 2010; Bassett et al., 2014). Hikurangi Plateau clays at Site 1124 contain over 8 wt.% water within the hydrous mineral phases (excluding water in pores) due to the presence of smectite (montmorillonite), heulandite, and clinoptilolite (Table 1, Appendix Table A.2). Fully hydrated montmorillonite with monovalent exchangeable cations contains ~7 wt.% water; fully hydrated montmorillonite with divalent exchangeable cations contains ~15 wt.% water. Montmorillonite in equilibrium with seawater comprises ~55% monovalent cations, and ~40-50% divalent cations and thus contains a total of ~11 wt.% interlayer water, which is released incrementally upon heating to ~180°C (172°C–192°C) (Sayles and Mangelsdorf, 1977; Colton-Bradley, 1987; Schleicher et al., 2015). Heulandite and clinoptilolite progressively lose 13–16 wt.% water up to ~350°C (Knowlton et al., 1981; Cruciani, 2006). Given a thermal gradient of ~12–15°C km^{-1} (Ellis et al., 2015), smectite dehydration would occur by ~12 km depth, but zeolite dehydration would continue until ~25 km depth. Depending on the permeability structure, fluids generated by dehydration reactions and compaction could lower the effective normal stress acting on the interface and promote slip (e.g., Fagereng and Ellis, 2009; Ellis et al., 2015).

Under conditions of hydrostatic pore-fluid pressure, shallow slip on the décollement will occur most efficiently within the stratigraphic unit with the lowest friction coefficient, which comprises Eocene clays at Site 1124, or a mélange containing this unit (Table 1) (e.g., Rowe et al., 2013). If Eocene clays act as impermeable seals (e.g., Faulkner, 2004), allowing the build-up of pore-fluid overpressures in underlying sediments, slip may also occur lower in the sequence. Slip in materials with higher friction coefficients becomes mechanically favourable when overpressures develop because pore-fluid pressure (P_p) reduces the apparent friction coefficient, μ_{app}, which is equal to $\tau/(\sigma_n - P_p)$. Pore fluid factors (λ) on the order of 0.7 to 0.8 would be required to make the μ_{app} of Late Paleocene chalks equivalent to those of Eocene clays containing hydrostatically pressured pore fluids (Table 1) (see also Burgreen-Chan et al., 2016). It should be noted that pore-fluid pressure variations not only affect apparent frictional strength, they also affect the relative strength ratio (α) in a compositionally heterogeneous mélange. While overpressure development in rate-weakening materials may lead to seismic slip, overpressure development in rate-strengthening material promotes aseismic creep (Equation 4) (Luo and Ampuero, 2017).

4.6 Relating experimental results to geodetic observations

Since 2002, New Zealand has benefitted from a continuous GPS network operated on behalf of several organisations by GeoNet (http://www.geonet.org.nz). Data from this network have allowed along-strike variations in interseismic coupling on the Hikurangi subduction interface to be mapped and have provided detailed coverage of spontaneously occurring as well as dynamically triggered slow slip events (SSEs) (Fig. 1) (e.g., Wallace et al., 2004, 2009, 2012, 2017; Douglas et al., 2005; Wallace and Beavan, 2010; Lamb and Smith, 2013;

Wei et al., 2018). From north-to-south, the geodetic locking depth progressively deepens — from less than ~15 km offshore the Gisborne and Hawke's Bay to ~30 km offshore south of Cape Turnagain (Fig. 1) (e.g., Wallace and Beavan, 2010; Wallace et al., 2012, 2018). Slow slip events are also segmented, occurring at <15 km depth on the northern and central décollement (East Coast SSEs, Fig. 1 of Wallace et al., 2012) and at >25–35 km depth on the southern décollement (Manawatu and Kapiti SSEs, Fig. 1 of Wallace et al., 2012). Along the central décollement, offshore Cape Turnagain, locking depth gradually increases, and the interface is partially coupled (Wallace et al., 2009, 2012).

Relating geodetic locking depth to fault rheology, i.e., the seismic-aseismic transition, requires two assumptions: (1) that decadal observations of fault behaviour are representative of long-term fault behaviour, and (2) that the geodetic locking depth is equal to, or at least approximates, the seismogenic locking zone depth, above which a given percentage of seismicity occurs (>~90%) (e.g., Nazareth and Hauksson, 2004; Jiang and Lapusta, 2017 and references therein). According to traditional models of crustal rheology, the lower limit of the seismogenic zone is governed by the onset of quartz plasticity, which occurs at 350°C; at lower temperatures, brittle quartz-rich rocks are expected to store elastic strain energy interseismically and release this energy coseismically (e.g., Goetze and Evans, 1979; Sibson, 1983; Scholz, 1988). Application of these models to the HSZ has proven unsuccessful because the transition to aseismic creep on the northern to central Hikurangi décollement occurs at temperatures as low as 100–150°C (McCaffrey et al., 2008; see also Fagereng and Ellis, 2009).

More recently, the shallow geodetic locking depth on the northern and central HSZ décollement was explained using a frictional-viscous rheology, whereby slip is accommodated by frictional sliding along aligned illite grains in series with thermally activated pressure solution of quartz clasts (Bos and Spiers, 2002; Fagereng and den Hartog, 2017). For a shear zone wider than 100 m containing moderate to high pore-fluid overpressure and 35/65 quartz/illite, the model successfully predicts a transition from (dilatant) frictional sliding to frictional-viscous flow at temperatures ≥100±20°C. With a thermal gradient of ~12–15°C km^{-1}, the transition to creep would occur at depths greater than ~6–10 km on the HSZ décollement (Ellis et al., 2015; Fagereng and den Hartog, 2017).

However, a frictional-viscous rheology does not explain interseismic coupling to approximately 30 km depth on the southern HSZ décollement, which is expected to have a similar thermal structure (e.g., Townend, 1997; Henrys et al., 2003; Fagereng and Ellis, 2009). Within the model framework, the along-strike variation can be explained if higher strain rates preclude pressure solution and deformation occurs instead via frictional sliding (Fagereng and den Hartog, 2017; Niemeijer, 2018). Yet outstanding questions remain about the applicability of a rheology based on the friction coefficient of illite, and the pressure solution kinetics of quartz, to the HSZ interface. Sediments studied herein contain primarily calcite, montmorillonite, and zeolite, with quartz comprising ≤5% of the interval sampled (Table 1, Appendix Table A.2). Calcareous sediments, rare (siliceous) cherts, and volcaniclastics dominate the Cretaceous-Paleogene input sequences recovered from ODP Leg 181 at Site 1124 and IODP Exp 375 at Sites U1520 and U1526 (Fig. 1, 2, 3) (Carter et al., 1999, 2004; Saffer et al., 2018).

Laboratory experiments were performed here on pelagic sediments from Site 1124 at velocities between 0.3 and 30 μm/s, at temperatures between 25°C and 225°C, and over durations less than 24 hours (Table 1) (Fig. 5). At these velocities, temperatures, and time scales, pressure solution of calcite is unlikely to have occurred quickly enough to accommodate deformation (Zhang et al., 2010; Chen et al., 2017). Microstructures indicate that deformation was accommodated frictionally via slip along anastomosing foliae in the clays and via localization and cataclasis in the chalks (Fig. 10). To correlate the frictional properties measured in the laboratory with geodetic observations, we employ rate-and-state friction theory. Rate-and-state friction theory states that rate-weakening behaviour promotes earthquake nucleation (and high interseismic coupling) and that rate-strengthening behaviour promotes aseismic creep (and low or neglible interseismic coupling) (e.g., Scholz, 1998; Avouac, 2015).

Frictionally, the stability of smectite-rich pelagic clays contrasts sharply with that of quartz and quartz-illite mixtures. Pure quartz and quartz/illite mixtures exhibit predominantly rate-strengthening behaviour at room temperature and become rate-weakening at temperatures ≥200-250°C and <400-500°C (Marone, 1998; Tembe et al., 2010; den Hartog et al., 2012b). In contrast, Site 1124 pelagic clays are rate-weakening to rate-neutral at low temperatures and become rate-strengthening at temperatures ≥150°C (Table 1). Because rate-strengthening behaviour promotes creep, a décollement with a matrix of montmorillonite, or its alteration product illite, would creep given sufficient driving stress, yielding a shallow geodetic locking depth of ~10-15 km (e.g., Saffer et al., 2001, 2012; Morrow et al., 2017; this study). The mapped locking depth on the central and northern HSZ décollement is consistent with the frictional properties of pelagic clays (Fig. 1). However, we have no data yet on the potential role(s) quartz and illite-rich sediments (i.e., turbidites), volcaniclastic sediments, and seamounts might play in modulating slip on the plate interface (e.g., Wang and Bilek, 2011; Wallace et al., 2012; Bell et al., 2014; Gao and Wang, 2014; Saffer and Wallace, 2015; Fagereng and den Hartog, 2017; Saffer et al., 2018).

The southern HSZ décollement is fully coupled and locked to a depth of 25–35 km, and paleoseismic records indicate that slip is accommodated in large-magnitude earthquakes (Wallace et al., 2009, 2012; Lamb and Smith, 2013; Clark et al., 2015). The rate-weakening behaviour of pelagic chalks is consistent with seismogenic behaviour at temperatures of 150°C and 225°C (Table 1); experiments performed previously at a wider range of temperatures and σ_n'=50 MPa show that calcite-rich gouges become rate-weakening at temperatures as low as 80°C, and remain frictionally unstable up to ~600°C at laboratory strain rates (Verberne et al., 2014, 2015). Lower effective normal stresses (σ_n'=10–30 MPa) promote rate-weakening behaviour at temperatures as low as ~20°C (e.g., Ikari et al., 2013; Tesei et al., 2014; Kurzawski et al., 2016). Thus, depending on effective normal stress, chalks (and their diagenetic equivalent, limestones) can exhibit rate-weakening behaviour at even the shallowest depths on the plate interface. Chalks consistently have higher friction coefficients than pelagic clays, so earthquake nucleation within them requires relatively higher driving stresses in the absence of pore-fluid overpressures.

The central HSZ décollement is only partially coupled. In the vicinity of Cape Turnagain, the coupling coefficient transitions from 0.8–1.0 beneath the southern North Island to 0.1–0.2 beneath the central to northern North Island (Fig. 1) (Wallace et al., 2004, 2009, 2012; Lamb and Smith, 2013). Along the central HSZ, the Manawatu SSEs occur on the interface at depths between 25 and 60 km, and the southernmost East Coast SSEs occur at less than ~15 km depth (Wallace et al., 2009, 2012, 2018). The transitional behaviour measured geodetically may reflect a heterogeneous distribution of rate-weakening and rate-strengthening lithologies and/or spatially variable pore-fluid pressures (Fagereng and Ellis, 2009; Wallace et al., 2012; Saffer and Wallace, 2015). Indeed, whether along-strike variations in geodetic locking depth, and slow slip events, reflect changes in lithologically controlled frictional properties, effective normal stress, fault zone structure (including roughness), or some combination of these variables, remains an active research question.

5. Conclusion

Stratigraphic, mineralogical and paleontological results show that hydrous clays containing zeolite were deposited at Site 1124 during the Eocene; clayey chalks and chalks occur above and below the clays. Experimentally, the frictionally weak clays are potentially unstable at T=25°C and T=75°C and become rate-strengthening at T≥150°C. Higher strength chalks exhibit the opposite trend, transitioning from rate-strengthening at T=25°C and T=75°C to rate-weakening at T≥150°C. At and above 150°C, the relative strength ratio (α) also increases, promoting seismic slip in a hydrostatically pressured fault comprising both types of sediment. Compositionally heterogeneous pelagic sediments exhibit contrasting, temperature-dependent frictional properties that can be correlated with variations in seismic style, although additional constraints on the on-fault distribution of rate-strengthening and rate-weakening lithologies are necessary to up-scale laboratory results. Data from deep-sea sediments at Site 1124 provide important spatial and temporal context for current and future Hikurangi Subduction Zone research.

Acknowledgements

This research used archival ODP samples provided by the International Ocean Discovery Program. The Royal Society of New Zealand supports C.B through a Rutherford Postdoctoral Fellowship, with additional funds provided by Victoria University of Wellington. ERC starting grant SEISMIC (335915) and the Netherlands Organization for Scientific Research (NWO) VIDI grant 854.12.011 supports A.R.N. This work was performed with assistance from the European Union’s Horizon 2020 Research and Innovation Programme, Grant Agreement N. 67654, Multi-scale laboratories Trans-national Access pilot, partly financed by NWO Internationalisation in the Earth and Life Sciences programme project number ALWIN.004. L. Hunfeld, T. Wolterbeek, E. de Graaf, and T. van der Gon Netscher provided excellent technical assistance. Results and data are tabulated in Table 1 and in Appendix A. Helpful discussions with S. Ellis and T. Little improved this manuscript. We thank F. Meneghini, M. Scuderi, and Editor P. Agard for constructive comments. The authors have no conflicts of interest.

References

Avouac, J.-P. (2015), From geodetic imaging of seismic and aseismic fault slip to dynamic modeling of the seismic cycle, *Annu. Rev. Earth Planet. Sci.*, *43*, 233-271.

Barker, D. H., R. Sutherland, S. Henrys, and S. Bannister (2009), Geometry of the Hikurangi subduction thrust and upper plate, North Island, New Zealand, *Geochem. Geophys. Geosyst., 10*(2), Q02007, doi:10.1029/2008GC002153.

Barnes, P. M., G. Lamarche, J. Bialas, S. Henrys, I. Pecher, G. L. Netzeband, J. Greiner, J. J. Mountjoy, K. Pedley, and G. Crutchley (2010), Tectonic and geological framework for gas hydrates and cold seeps on the Hikurangi subduction margin, New Zealand, *Marine Geol.*, *272*, 26-48.

Bartlow, N. M., S. I. Myazaki, A. M. Bradley, and P. Segall (2011), Space-time correlation of slip and tremor during the 2009 Cascadia slow slip event. *Geophys. Res. Lett.*, *38*, doi:10.1029/2011GL048714.

Bassett, D., R. Sutherland, and S. Henrys (2014), Slow wavespeeds and fluid overpressure in a region of shallow locking and slow slip, Hikurangi subduction margin, New Zealand, *Earth Planet. Sci. Lett.*, *389*, 1-13.

Behnsen, J., and D. R. Faulkner (2013), Permeability and frictional strength of cation-exchanged montmorillonite, *J. Geophys. Res. Solid Earth*, *118*, 1-11, doi:10.1002/jgrb.50226.

Bell, R., C. Holden, W. Power, X. Wang, and G. Downes (2014), Hikurangi margin tsunami earthquake generated by slow seismic rupture over a subducted seamount, *Earth Planet. Sci. Lett.*, *397*, 1-9.

Bell, R., R. Sutherland, D. H. N. Barker, S. Henrys, S. Bannister, L. Wallace, and J. Beavan (2010), Seismic reflection character of the Hikurangi subduction interface, New Zealand, in the region of repeated Gisborne slow slip events, *Geophys. J. Int.*, *180*, 34-48.

Bijl, P.K., S. Schouten, A. Sluijs, G.-J. Reichart, J. C. Zachos, and H. Brinkhuis (2009), Early Paleogene temperature evolution of the southwest Pacific Ocean, *Nature*, *461*, 776-779.

Blanpied, M. L., D. A. Lockner, and J. D. Byerlee (1995). Frictional slip of granite at hydrothermal conditions. *J. Geophys. Res.*, *100*(B7), 13045-13064.

Blanpied, M. L., T. E. Tullis, and J. D. Weeks (1998). Effects of slip, slip rate, and shear heating on the friction of granite. *J. Geophys. Res.*, *103*(B1), 489-511.

Bos, B., and C. J. Spiers (2002), Frictional-viscous flow of phyllosilicate-bearing fault rock: Microphysical model and implications for crustal strength profiles, *J. Geophys. Res.*, *107*(B2), 2028, doi:10.1029/2001JB000301.

Bos, B., and C. J. Spiers (2001), Experimental investigation into the microstructural and mechanical evolution of phyllosilicate-bearing fault rock under conditions favouring pressure solution*, J. Struct. Geol.*, *23*(8), 1187-2002.

Bown, P. R., and J. R. Young (1998), Techniques, in *Calcareous Nannofossil Biostratigraphy*, edited by P.R. Bown, 16-28, Kluwer Academie, London.

Bullock, R. J., N. De Paola, and R. E. Holdsworth (2015), An experimental investigation into the role of phyllosilicate content on earthquake propagation during seismic slip in carbonate faults, *J. Geophys. Res. Solid Earth*, *120*, 3187-3207, doi:10.1002/2015JB011914.

Burgreen-Chan, B., K. E. Meisling, and S. Graham (2016), Basin and petroleum system modelling of the East Coast Basin, New Zealand: a test of overpressure scenarios in a convergent margin, *Basin Research*, *28*, 536-567, doi:10.1111/bre.12121.

Carter, R. M., I. N. McCave, and L. Carter (2004), Leg 181 synthesis: fronts, flows, drifts, volcanoes, and the evolution of the southwestern gateway to the Pacific Ocean, eastern New Zealand, in *Proceedings of the Ocean Drilling Program, Scientific Results*, *181*, edited by C. Richter, 1-111, doi:10.2973/odp/proc.sr.181.210.2004.

Carter, R. M., I. N. McCave, C. Richter, L. Carter, et al. (1999), *Proceedings of the Ocean Drilling Program, Initial Reports, 181*, College Station, TX (Ocean Drilling Program), 1-80, doi:10.2973/odp.proc.ir.181.101.2000.

Chen, J., and C.J. Spiers (2016). Rate and state frictional and healing behaviour of carbonate fault gouge explained using microphysical model. *J. Geophys. Res. Solid Earth*, *121*, 8642-8665, doi:10.1002/2016JB013470.

Chen, J., B. A. Verberne, and C. J. Spiers (2015), Effects of healing on the seismogenic potential of carbonate fault rocks: Experiments on samples from the Longmenshan Fault, Sichuan, China. *J. Geophys. Res. Solid Earth*, *120*, 5479–5506. doi:10.1002/2015JB012051.

Chen, J., A. R. Niemeijer, and C. J. Spiers (2017), Microphysically derived expressions for rate-and-state friction parameters, *a*, *b*, and D_c, *J. Geophys. Res. Solid Earth*, *122*, 9627-9657, doi:10.1002/2017JB014226.

Chester, F., C. Rowe, K. Ujiie, et al. (2013), Structure and composition of the plate-boundary slip zone for the 2011 Tohoku-Oki earthquake, *Science*, *342*(6163), 1208-1211, doi:10.1126/science.1243719.

Clark, K. J., B. W. Hayward, U. A. Cochran, L. M. Wallace, W. L. Power, and A. T. Sabaa (2015), Evidence for past subduction earthquakes at a plate boundary with widespread upper plate faulting: Southern Hikurangi Margin, New Zealand, *Bull. Seis. Soc. Am.*, *105*(3)*, 1661-1690*, doi:10.1785/0120140291.

Cloos, M., and R.L. Shreve (1988), Subduction-channel model of prism accretion, mélange formation, sediment subduction, and subduction erosion at convergent plate margins: 1. Background and Description, *Pure Appl. Geophys*., *128*(3/4), 455-500.

Collettini, C., A. Niemeijer, C. Viti, and C. Marone (2009), Fault zone fabric and fault weakness, *Nature*, 462, 907-911.

Colton-Bradley, V. A. (1987), Role of pressure in smectite dehydration—Effects on geopressure and smectite-to-illite transformation, *Am. Assoc. Pet. Geol. Bull.*, *71*(11), 1414-1427.

Crouch, E. M., and H. Visscher (2003), Terrestrial vegetation record across the initial Eocene thermal maximum at the Tawanui marine section, New Zealand. *Spec. Pap. Geol. Soc. Am.*, *369*, 351-363.

Cruciani, G. (2006), Zeolites upon heating: Factors governing their thermal stability and structural changes, *J. Phys. Chem. Solids*, *67,* 1973-1994.

Davy, B., K. Hoernle, and R. Werner (2008), Hikurangi Plateau: Crustal structure, riften formation, and Gondwana subduction history, *Geochem. Geophys. Geosys.*, *9*(7), Q07004, doi:10.1029/2007GC001855.

Dean, W. E., M. Leinen, and D. A. V. Stow (1985), Classification of deep-sea, fine-grained sediments, *J. Sediment. Petrol.*, *55*(2), 250-256.

Delahaye, E. J., J. Townend, M. E. Reyners, and G. Rodgers (2009), Microseismicity but no tremor accompanying slow slip in the Hikurangi subduction zone, New Zealand, *Earth Planet. Sci. Lett.*, *277*, 21-28.

den Hartog, S. A. M., A. R., Niemeijer, and C. J. Spiers (2012a). New constraints on mega-thrust slip stability under subduction zone P-T conditions. *Earth Planet. Sci. Lett.*, *353–354*, 240–252.

den Hartog, S. A. M., C. J. Peach, D. A. M. de Winter, C. J. Spiers, and T. Shimamoto (2012b), Frictional properties of megathrust fault gouges at low sliding velocities: New data on effects of normal stress and temperature, *J. Struct. Geol.*, *38*, 156-171.

Dieterich, J. (1979), Modeling of rock friction 1. Experimental results and constitutive equations, *J. Geophys. Res*, *84*(B5), 2162-2168, doi:10.1029/JB084iB05p02151.

Doser, D. I., and T. H. Webb (2003), Source parameters of large historical (1917-1961) earthquakes, North Island, New Zealand, *Geophys. J. Int.*, *152*, 795-832.

Douglas, A., J. Beavan, L. Wallace, and J. Townend (2005), Slow slip on the northern Hikurangi subduction interface, New Zealand, *Geophys. Res. Lett.*, *32*, L16305, doi:10.1029/2005GL023607.

Eberhart-Phillips, D., and S. Bannister (2015), 3-D imaging of the northern Hikurangi subduction zone, New Zealand: variations in subducted sediment, slab fluids and slow slip, *Geophys. J. Int.*, *201*, 838-855, doi:10.1093/gji/ggv057.

Ellis, S., A. Fagereng, D. Barker, S. Henrys, D. Saffer, L. Wallace, C. Williams, and R. Harris (2015), Fluid budgets along the northern Hikurangi subduction margin, New Zealand:

the effect of a subducting seamount on fluid pressure, *Geophys. J. Int.*, *202*, 277-297, doi:10.1093/gji/ggv127.

Fagereng, Å. (2013), On stress and strain in a continuous-discontinuous shear zone undergoing simple shear and volume loss, *J. Struct. Geol.*, *50*, 44-53.

Fagereng, Å. (2011a), Wedge geometry, mechanical strength, and interseismic coupling of the Hikurangi subduction thrust, New Zealand, *Tectonophys.*, *506*, 26-30.

Fagereng, Å. (2011b), Frequency-size distribution of competent lenses in a block-in-matrix mélange: Imposed length scales of brittle deformation? *J. Geophys. Res.*, *116*, B05302, doi:10.1029/2010JB007775.

Fagereng, Å., and S. Ellis (2009), On factors controlling the depth of interseismic coupling on the Hikurangi subduction interface, New Zealand, *Earth Planet. Sci. Lett.*, *278*(1-2), 120-130.

Fagereng, Å., and R. H. Sibson (2010), Mélange rheology and seismic style, *Geology*, *38*(8), 751-754, doi:10.1130/G30868.

Fagereng, Å. & den Hartog, S.A.M., 2017. Subduction megathrust creep governed by pressure solution and frictional-viscous flow. Nature Geoscience 10, doi:10.1038/NGEI2857.

Faulkner, D. R. (2004), A model for the variation in permeability of clay-bearing fault gouge with depth in the brittle crust, *Geophys. Res. Lett.*, *31*, L19611, doi:10.1029/2004GL020736.

Faulkner, D. R., C. Sanchez-Roa, C. Boulton, and S. A. M. den Hartog (2018), Pore fluid pressure development in compacting fault gouge in theory, experiment, and nature, *J. Geophys. Res. Solid Earth*, *123*, doi:10.1002/2017JB015130.

Faulkner, D.R., T. M. Mitchell, J. Behnsen, T. Hirose, and T. Shimamoto (2011), Stuck in the mud? Earthquake nucleation and propagation through accretionary forearcs, *Geophys. Res. Lett.*, *38*, L18303, doi:10.1029/2011GL048552.

Field, B. D., C. I. Uruski, A. Beu et. al. (1997), *Cretaceous-Cenozoic geology and petroleum systems of the East Coast Region. Institute of Geological and Nuclear Sciences monograph 19*, 301 pp., Institute of Geological and Nuclear Sciences Limited, Lower Hutt.

Gao, X., and K. Wang (2014), Strength of stick-slip and creeping subduction megathrusts from heat flow observations, *Science*, *345*(6200), 1038-1041, doi:10.1126/science.1255487.

Ghisetti, F.C., P. M. Barnes, S. Ellis, A. A. Plaza-Faverola, and D. H. N. Barker (2016), The last 2 Myr of accretionary wedge construction in the central Hikurangi margin (North Island, New Zealand): Insights from structural modelling, *Geochem. Geophys. Geosys.*, doi:10.1002/2016GC006341.

Giorgetti, C., B. M. Carpenter, and C. Collettini (2015), Frictional behaviour of talc-calcite mixtures, *J. Geophys. Res. Solid Earth*, *120*, doi:10.1002/2015JB011970.

Goetze, C., and B. Evans (1979), Stress and temperature in the bending lithosphere as constrained by experimental rock mechanics, *Geophys. J. Int.*, *59*(3), 463-478.

Gradstein, F. M., J. G. Ogg, M. Schmitz, and G. Ogg (2012), *The Geological Time Scale*, Elsevier, Amsterdam.

Gratier, J.-P., F. Thouvenot, L. Jenetton, A. Tourette, M.-L. Doan, and F. Renard (2013), Geological control of the partitioning between seismic and aseismic sliding behaviours in active faults: Evidence from the Western Alps, France, *Tectonophys.*, *600*, 226-242.

Gu, J.-C., J. R. Rice, A. L. Ruina, and S. T. Tse (1984), Slip motion and stability of a single degree of freedom elastic system with rate and state dependent friction, *J. Mech. Phys. Solids*, *32*(3), 167-196.

Heise, W., T. G. Caldwell, S. Bannister, E. A. Bertrand, Y. Ogawa, S. L. Bennie, H. Ichihara (2017), Mapping subduction interface coupling using magnetotellurics: Hikurangi margin, New Zealand, *Geophys. Res. Lett.*, 44(18), 9261-9266.

Henrys, S. A., S. Ellis, and C. Uruski (2003), Conductive heat flow variations from bottom-simulating reflectors on the Hikurangi margin, New Zealand, *Geophys. Res. Lett.*, *30*(2), *1065*, doi:10.1029/2002GL015772.

Hillier, S. (1995), Erosion, sedimentation and sedimentary origin of clays, in, *Origin and Mineralogy of Clays*, edited by B. Velde, 162-214, Springer-Verlag, Berlin.

Hines, B. R., D. K. Kulhanek, C. J. Hollis, C. B. Atkins, and H. E. G. Morgans (2013), Paleocene-Eocene stratigraphy and paleoenvironment at Tora, Southeast Wairarapa, New Zealand, *N. Z. J. Geol. Geophys.*, *56*(4), 243-262.

Hollis, C. J., K. W. R. Taylor, L. Handley, et al. (2012), Early Paleogene temperature history of the Southwest Pacific Ocean: Reconciling proxies and models, *Earth Planet. Sci. Lett.*, *349-350*, 53-66.

Hollis, C. J., G. R. Dickens, B. D. Field, C. J. Jones, and C. P. Strong (2005a), The Paleocene-Eocene transition at Mead Stream, New Zealand: a southern Pacific record of early Cenozoic global change, *Palaeogeogr., Palaeoclimatol., Palaeoecol.*, *215*, 313-343.

Hollis, C. J., B. D. Field, C. M. Jones, C. P. Strong, G. J. Wilson, and G. R. Dickens (2005b), Biostratigraphy and carbon isotope stratigraphy of uppermost Cretaceous-lower Cenozoic in middle Clarence valley, New Zealand, *J. Roy. Soc. N. Z.*, *35*(3), 345-383.

Ikari, M. J., A. R. Niemeijer, C. J. Spiers, A. J. Kopf, and D. M. Saffer (2013), Experimental evidence linking slip instability with seafloor lithology and topography at the Costa Rica convergent margin, *Geology*, *41*(8), 891-894, doi:10.1130/G33956.1.

Ikari, M. J., D. M. Saffer, and C. Marone (2009), Frictional and hydrologic properties of clay-rich fault gouge, *J. Geophys. Res.*, *114*, B05409, doi:10.1029/2008JB006089.

Jiang, J., and N. Lapusta (2017), Connecting depth limits of interseismic locking, microseismicity, and large earthquakes in models of long-term fault slip, *J. Geophys. Res. Solid Earth*, *122*, 6491-6253, doi:10.1002/2017JB014030.

Kastner, M. (1999), Oceanic minerals: their origin, nature of their environment, and significance, *Proc. Natl. Acad. Sci. USA*, *96*, 3380-3387.

Kastner, M. (1981), Authigenic silicates in deep-sea sediments: Formation and diagenesis, in, *The sea*, vol. 7, edited by C. Emiliani, 915-980, Wiley, New York.

Kilgore, B. D., M. L. Blanpied, and J. H. Dieterich (1993), Velocity dependent friction of granite over a wide range of conditions, *Geophys. Res. Lett*., *20*(10), 903-906.

Kimura, G., A. Yamaguchi, M. Hojo, et al. (2012), Tectonic mélange as fault rock of subduction plate boundary, *Tectonophys.*, *568-569*, 25-38.

Kitajima, H., and D. M. Saffer (2012), Elevated pore pressure and anomalously low stress in regions of low frequency earthquakes along the Nankai Trough subduction megathrust, *Geophys. Res. Lett.*, *39*, L23301, doi:10.1029/2012GL053793.

Knowlton, G. D., T. R. White, and H. L. McKague (1981), Thermal study of types of water associated with clinoptilolite, *Clays. Clay Miner.*, *29*, 403-411.

Kurzawski, R. M., M. Stipp, A. R. Niemeijer, C. J. Spiers, and J. H. Berhmann (2016), Earthquake nucleation in weak subducted carbonates, *N. Geosci.*, *9*, 717-723.

Lamb, S., and E. Smith (2013), The nature of the plate interface and driving force of interseismic deformation in the New Zealand plate-boundary zone, revealed by the continuous GPS velocity field, *J. Geophys. Res. Solid Earth*, *118*, 1-30, doi:10.1002/jgrb.50221.

Leeman, J. R., D. M Saffer, M. M. Scuderi, and C. Marone (2016), Laboratory observations of slow earthquakes and the spectrum of tectonic fault slip modes, *Nat. Comm.*, *7*, 1-6, doi:10.1038/ncomms11104.

Logan, J. M., C. A. Dengo, N. G. Higgs, Z. Z. Wang (1992), Fabrics of experimental fault zones: their development and relationship to mechanical behaviour, in, *Fault mechanics and transport properties of rocks*, edited by B. Evans and T.F. Wong, Academic Press, New York, 33-68.

Liu, Y., and J. R. Rice (2007), Spontaneous and triggered aseismic deformation transients on a subduction fault model, *J. Geophys. Res.*, *112*, B09404, doi:10.1038/ncomms13020.

Luo, Y., and J.-P. Ampuero (2017), Stability of faults with heterogeneous friction properties and effective normal stress, *Tectonophys.*, doi:10.1016/j.tecto.2017.11.006.

Maltman, A. (Ed.) (1994), *The Geological Deformation of Sediments*, Springer, 307 pp.

Marone, C. (1998), Laboratory-derived friction laws and their application to seismic faulting, *Annu. Rev. Earth Planet. Sci.*, *26*, 643-696.

Martini, E. (1971), Standard Tertiary and Quaternary calcareous nannoplankton zonation, in, *Proceedings of the Second Planktonic Conference Roma 1970*, edited by A. Farinacci, Edizioni Tecnoscienza, Rome, 2, 739–785.

McCaffrey, R., L. M. Wallace, and J. Beavan (2008), Slow slip and frictional transition at low temperature at the Hikurangi subduction zone, *N. Geosci.*, *1*, 316-320.

McLaskey, G. C., and F. Yamashita (2017), Slow and fast ruptures on a laboratory fault controlled by loading characteristics, *J. Geophys. Res. Solid Earth*, *122*, 3719-3738, doi:10.1002/2016JB013681.

Mittempergher, S., A. Cerchiari, F. Remitti, and A. Festa (2018), From soft sediment deformation to fluid assisted fault in the shallow part of a subduction megathrust analogue: the Sestola Vidiciatico tectonic unit (Northern Apennines, Italy), *Geol. Mag.*, *155*(2), 438-450, doi:10.1017/S0016756817000668.

Moore, D. E., and D. A. Lockner (2007), Friction of the smectite clay montmorillonite: A review and interpretation of data, in, *The Seismogenic Zone of Subduction Thrust Faults, Margins Theoretical and Experimental Earth Science Series*, vol. 2, edited by T. H. Dixon and C. Moore, pp. 317-345, Columbia Univ. Press, New York.

Morrow, C.A., D.E. Moore, and D.A. Lockner (2017), Frictional strength of wet and dry montmorillonite, *J. Geophys. Res. Solid Earth*, *122*, 3392-3409, doi:10.1002/2016JB013658.

Mumpton, F. A. (1960), Clinoptilolite redefined, *Am. Mineral.*, *45*, 351-369.

Muzutani, T., K.-i. Hirauchi, W. Lin, and M. Sawai (2017), Depth dependence of the frictional behaviour of montmorillonite fault gouge: Implications for seismicity along a decollement zone, *Geophys. Res. Lett.*, *44*, 5383-5390, doi:10.1002/2017GL073465.

Nakatani, M. (2001), Conceptual and physical clarification of rate and state friction: Frictional sliding as a thermally activated rheology, *J. Geophys. Res.*, *106*(B7), 13347-13380, doi:10.1029/2000JB900453.

Nazareth, J. J., and E. Haukkson (2004), The seismogenic thickness of the Southern California crust, *Bull. Seismol. Soc. Am.*, *94*(3), 940-960.

Nicolo, M. J., G. R. Dickens, C. J. Hollis, and J. C. Zachos (2007), Multiple early Eocene hyperthermals: Their sedimentary expression on the New Zealand continental margin and in the deep sea, *Geology*, *35*(8), 699-702, doi:10.1130/G23648A.1.

Niemeijer, A.R. (2018), Velocity-dependent slip weakening by the combined operation of pressure and foliation development, *Nature Sci. Rep.*, *8*, 4724, doi:10.1038/s41598-018-22889-3.

Niemeijer, A. R., and C. J. Spiers (2006), Velocity dependence of strength and healing behaviour in simulated phyllosilicate-bearing fault gouge. *Tectonophys.*, *427*, 231-253, doi:10.1016/j.tecto.2006.03.048.

Niemeijer, A. R., C. J. Spiers, and C. J. Peach (2008), Frictional behaviour of simulated quartz fault gouges under hydrothermal conditions: Results from ultra-high strain rotary shear experiments, *Tectonophys., 460*, 288-303.

Pedley, K. L., P. M. Barnes, J. R. Pettinga, and K. B. Lewis (2010), Seafloor structural geomorphic evolution of the accretionary frontal wedge in response to seamount subduction, Poverty Indentation, New Zealand, *Marine Geol.*, *270*, 119-138.

Peng, Z., and J. Gomberg (2010), An integrated perspective of the continuum between earthquakes and slow-slip phenomena, *Nat. Geosci.*, *3*, 599-607, doi:10.1038/ngeo940.

Plank, T. (2014), The chemical composition of subducting sediments, *Treatise on Geochemistry (Second Edition)*, *4*, 607-629, doi:10.1016/B978-0-08-095975-7.00319-3.

Plank, T., and C. H. Langmuir (1998), The chemical composition of subducting sediment and its consequences for the crust and mantle, *Chem. Geol*., *145*, 325-394.

Plaza-Faverola, A., S. Henrys, I. Pecher, L. Wallace, and D. Klaeschen (2016), Splay fault branching from the Hikurangi subduction shear zone: Implications for slow slip and fluid flow, *Geochem. Geophys. Geosys.*, *17*, 5009-5023, doi:10.1002/2016GC006563.

Plaza-Faverola, A., D. Klaeschen, P. Barnes, I. Pecher, S. Henrys, and J. Mountjoy (2012), Evolution of fluid expulsion and concentrated hydrate zones across the southern Hikurangi subduction margin, New Zealand: An analysis from depth migrated seismic data, *Geochem. Geophys. Geosys.*, *13*(8), Q08018, doi:10.1029/2012GC004228.

Pluymakers, A., J. E. Samuelson, A. R. Niemeijer, and C. J. Spiers, C.J. (2014), Effects of temperature and CO_2 on the frictional behavior of simulated anhydrite fault rock, *J. Geophys. Res. Solid Earth*, *119*(12), 8728–8747. doi:10.1002/2014JB011575.

Rabinowitz, H. S., H. M. Savage, R. M. Skarbek, et al. (2018), Frictional behavior of input sediments to the Hikurangi Trench, New Zealand, *Geochem. Geophys. Geosys.*, doi:10.1029/2018GC007633.

Rowe, C., J. C. Moore, F. Remitti, and IODP Expedition 343/343T Scientists (2013), The thickness of subduction plate boundary faults from the seafloor into the seismogenic zone, *Geology*, *41*(9), 991-994, doi:10.1130/G34556.1.

Rubin, A. M. (2008), Episodic slow slip events and rate-and-state friction, *J. Geophys. Res.*, *113*, B11414, doi:10.1029/2008JB005642.

Ruina, A. (1983), Slip instability and state variable laws, *J. Geophys. Res*., *88*(B12), 10359-10370, doi:10.1029/JB088iB12p10359.

Saffer, D. M., and L. M. Wallace (2015), The frictional, hydrologic, metamorphic and thermal habitat of shallow slow earthquakes, *Nat. Geosci.*, *8*, 594-600, doi:10.1038/NGEO2490.

Saffer, D. M., and C. Marone (2003), Comparison of smectite- and illite-rich gouge frictional properties: Application to the updip limit of the seismogenic zone along subduction megathrusts, *Earth Planet. Sci. Lett.*, *251*(1-2), 219-235, doi:10.1016/S0012-821X(03)0042-2.

Saffer, D. M., L. M. Wallace, K. Petronotis, and the Expedition 375 Scientists (2018), *Expedition 375 Preliminary Report: Hikurangi Subduction Margin Coring and Observatories*. International Ocean Discovery Program, doi:10.14379/iodp.pr.375.2018.

Saffer, D. M., D. A. Lockner, and A. McKiernan (2012), Effects of smectite to illite transformation on the frictional strength and sliding stability of intact marine mudstones, *Geophys. Res. Lett*., *39*, L11304, doi:10.1029/2012GL051761.

Saffer, D. M., K. M. Frye, C. Marone, and K. Mair (2001), Laboratory results indicating complex and potentially unstable frictional behaviour of smectite clay, *Geophys. Res. Lett.*, *28*, 2297-2300, doi:10.1029/2001GL012869.

Sakuma, H., and S. Suehara (2015), Interlayer bonding energy of layered minerals: Implication for the relationship with friction coefficient, *J. Geophys. Res. Solid Earth*, *120*, 2212-2219, doi:10.1002/2015JB011900.

Sammis, C. G., and S. J. Steacy (1994), The micromechanics of friction in a granular layer, *Pure Appl. Geophys*., *142*(3/4), 778-794.

Samuelson, J., D. Elsworth, and C. Marone (2010), Shear-induced dilatancy of fluid-saturated faults: Experiment and theory, *J. Geophys. Res.*, *114*, B12404, doi:10.1029/2008JB006273.

Sanchez-Roa, C., D. R. Faulkner, C. Boulton, J. Jimenez-Millan, and F. Nieto (2017), How phyllosilicate mineral structure affects fault strength in Mg-rich fault systems, *Geophys. Res. Lett.*, 44, doi:10.1002/2017GL073055.

Sawai, M., A. R. Niemeijer, T. Hirose, and C. J. Spiers (2017), Frictional properties of JFAST core samples and implications for slow earthquakes at the Tohoku subduction zone, *Geophys. Res. Lett.*, *44*, 8822-8831, doi:10.1002/2017GL073460.

Sayles, F. L., and P. C. Mangelsdorf, Jr. (1977), The equilibration of clay minerals with sea water: exchange reactions, *Geochim. Cosmochim. Acta*, *41*(7), 951-960.

Schleicher, A. M., A. Boles, and B. A. van der Pluijm (2015), Response of natural smectite to seismogenic heating and potential implications for the 2011 Tohoku earthquake in the Japan Trench, *Geology*, *43*(9), 755-758.

Scholz, C. H. (1998), Earthquakes and friction laws, *Nature*, *391*, 37-42.

Scholz, C. H. (1988), the brittle-plastic transition and the depth of seismic faulting, *Geol. Rundsch.*, *77*, 319-328.

Schwartz, S. Y., and J. M. Rokosky (2007), Slow slip events and seismic tremor at circum-Pacific subduction zones. *Rev. Geophys.*, *45*, doi:10.1029/2006gr000208.

Segall, P., A. M. Rubin, A. M. Bradley, and J. R. Rice (2010), Dilatant strengthening as a mechanism for slow slip events, *J. Geophys. Res.*, *115*, B12305, doi:10.1029/2010JB007449.

Sibson, R.H. (1983), Continental fault structure and the shallow earthquake source, *J. Geol. Soc. Lond.*, *140*, 741-767.

Skarbek, R. M., and A.W. Rempel (2017), Heterogeneous Coloumb wedges: Influence of fluid pressure, porosity, and application to the Hikurangi subduction margin, New Zealand. *J. Geophys. Res. Solid Earth*, *122*, 1585-1613, doi:10.1002/2016JB013497.

Skarbek, R. M., A. W. Rempel, and D. A. Schmidt (2012), Geologic heterogeneity can produce aseismic slip transients, *Geophys. Res. Lett.*, *39*, L21306, doi:10.1029/2012GL053762.

Slotnick, B. S., G. R. Dickens, C. J. Hollis, J. S. Crampton, C. Percy Strong, and A. Phillips (2015), The onset of the Early Eocene Climatic Optimum at Branch Stream, Clarence River valley, New Zealand, *N. Z. J. Geol. Geophys.*, *58*(3), 262-280.

Slotnick, B. S., G. R. Dickens, M. Nicolo, C. J. Hollis, J. S. Crampton, J. C. Zachos, and A. Sluijs (2012), Numerous large amplitude variations in carbon cycling and terrestrial weathering throughout the latest Paleocene and earliest Eocene, *J. Geol.*, *120*(5), 487-505.

Smith, S. A., F., and D. R. Faulkner (2010), Laboratory measurements of the frictional properties of the Zuccale low-angle normal fault, Elba Island, Italy, *J. Geophys. Res*., *115*, B02407, doi:10.1029/2008JB006274.

Tembe, S., D. A. Lockner, and T.-F. Wong (2010), Effect of clay content and mineralogy on frictional sliding behaviour of simulated gouges: Binary and ternary mixtures of quartz, illite, and montmorillonite, *J. Geophys. Res.*, *115*, B03416, doi:10.1029/2009JB006383.

Tesei, T., C. Collettini, M. R. Barchi, B. M. Carpenter, and G. Di Stefano (2014), Heterogeneous strength and fault zone complexity of carbonate-bearing thrusts with possible implications for seismicity, *Earth Planet. Sci. Lett.*, *408*, 307-318.

Thiry, M. (2000), Paleoclimatic interpretation of clay minerals in marine deposits: an outlook from the continental origin, *Earth Sci. Rev.*, *49*, 201-221.

Todd, E. K., and S. Y. Schwartz (2016), Tectonic tremor along the northern Hikurangi Margin, New Zealand, between 2010 and 2015, *J. Geophys. Res. Solid Earth*, *121*, 8706-8719, doi:10.1002/2016JB013480.

Townend, J. (1997), Estimates of conductive heat flow through bottom-simulating reflectors at the Hikurangi and southwest Fiordland continental margins, *N. Z. Mar. Geol.*, *141*, 209-220.

Verberne, B. A., A. R. Niemeijer, J. H. P. De Bresser, and C. J. Spiers (2015), Mechanical behavior and microstructure of simulated calcite fault gouge sheared at 20-600C: Implications for natural faults in limestones, *J. Geophys. Res. Solid Earth*, *120*, doi:10.1002/2015JB012292.

Verberne, B. A., C. J. Spiers, A. R. Niemeijer, J. H. P. De Bresser, D. A. M. De Winter, and O. Plumper (2014), Frictional properties and microstructure of calcite-rich fault gouges sheared at sub-seismic sliding velocities, *Pure Appl. Geophys*., *171*(10), 2617-2640.

Wallace, L. M., and J. Beavan (2010), Diverse slow slip behaviour at the Hikurangi subduction margin, New Zealand. *J. Geophys. Res.*, *115*, B12402, doi:10.1029/2010JB00771.

Wallace, L. M., S. Hreinsdóttir, S. Ellis, I. Hamling, E. D'Anastasio, and P. Denys (2018), Triggered slow slip and afterslip on the southern Hikurangi Subduction Zone following the Kaikoura Earthquake, *Geophys. Res. Lett., 45*, 4710-4718, doi:10.1002/2018GL077385.

Wallace, L. M., Y. Kaneko, S. Hreinsdóttir, et al. (2017), Large-scale dynamic triggering of shallow slow slip enhanced by overlying sedimentary wedge, *Nat. Geosci.*, doi:10.1038/NGEO3021.

Wallace, L. M., J. Beavan, S. Bannister, and C. Williams (2012), Simultaneous long-term and short-term slip events at the Hikurangi subduction margin, New Zealand: Implications for processes that control slow slip occurrence, duration, and migration, *J. Geophys. Res. 117*(B11402), doi:10.1029/2012JB009489.

Wallace, L. M., M. Reyners, U. Cochran, et al. (2009), Characterizing the seismogenic zone of a major plate boundary subduction thrust: Hikurangi Margin, New Zealand, *Geochem. Geophys. Geosys.*, *10*(10), Q10006.

Wallace, L. M., J. Beavan, R. McCaffrey, and D. Darby (2004), Subduction zone coupling and tectonic block rotations in the North Island, New Zealand. *J. Geophys. Res.*, *109*, B12406, doi:10.1029/2004JB003241.

Wang, K., and S. L. Bilek (2011), Do subducting seamounts generate or stop large earthquakes?, *Geology*, *39*(9), 819-822.

Wei, M., Y. Kaneko, P. Shi, and Y. Liu (2018), Numerical modelling of dynamically triggered slow slip events in New Zealand by the 2016 Mw 7.8 Kaikoura Earthquake, *Geophys. Res. Lett.*, *45*, doi:10.1029/2018GL077879.

Zachos, J. C., U. Röhl, S. A. Schellenberg, et al. (2005), Rapid acidification of the ocean during the Paleocene-Eocene Thermal Maximum, *Science*, *308*, 1611-1615, doi:10.1126/science.1109004.

Zhang, X., C. J. Spiers, and C. J. Peach (2010), Compaction creep of wet granular calcite by pressure solution at 28C to 150C. J. Geophys. Res., 115, B09217

Figures

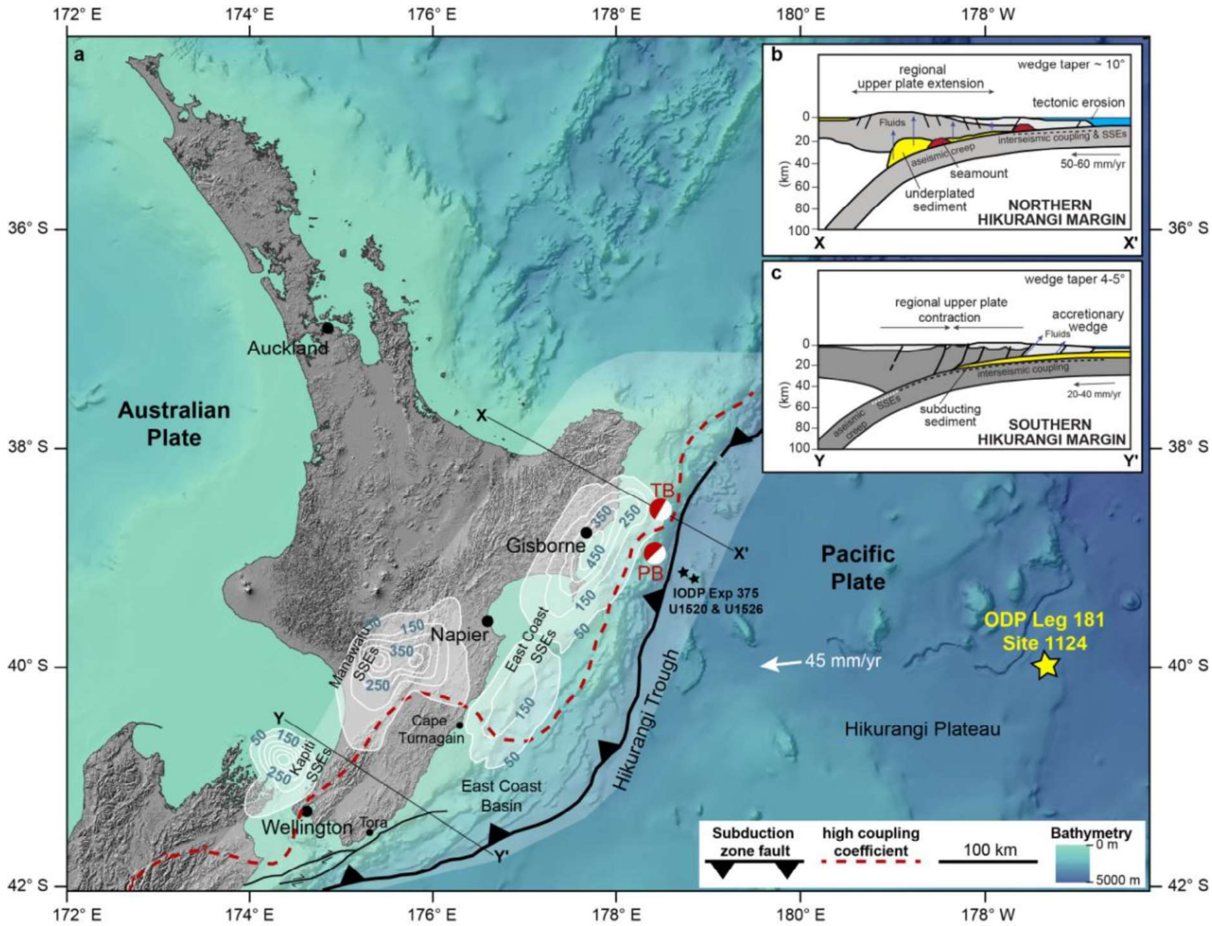

Figure 1. (a) Location of the Hikurangi Subduction Zone (HSZ), North Island, New Zealand, and ODP Site 1124. Contours on the décollement quantify the net slip accommodated by slow slip events between 2002 and 2012 (after Wallace et al., 2012). Regions up dip of the red dashed line are highly coupled and accumulating elastic strain energy (after Wallace et al., 2012). Earthquake focal mechanisms are from Doser and Webb (2003): PB is Poverty Bay (25 March 1947) and TB is Tokomaru Bay (17 May 1947). Lightly shaded region defines the East Coast Basin. **(b)** Cartoon cross-section through the northern HSZ, depicting the roughness of the downgoing plate, relatively higher wedge taper angle, and underplating sediment, as well as extension in the overriding plate (modified after Wallace et al., 2009). **(c)** Cartoon cross-section through the southern HSZ, depicting a relatively smooth downgoing plate with a low wedge taper angle, subducting sediment, and compression in the overriding plate (modified after Wallace et al., 2009).

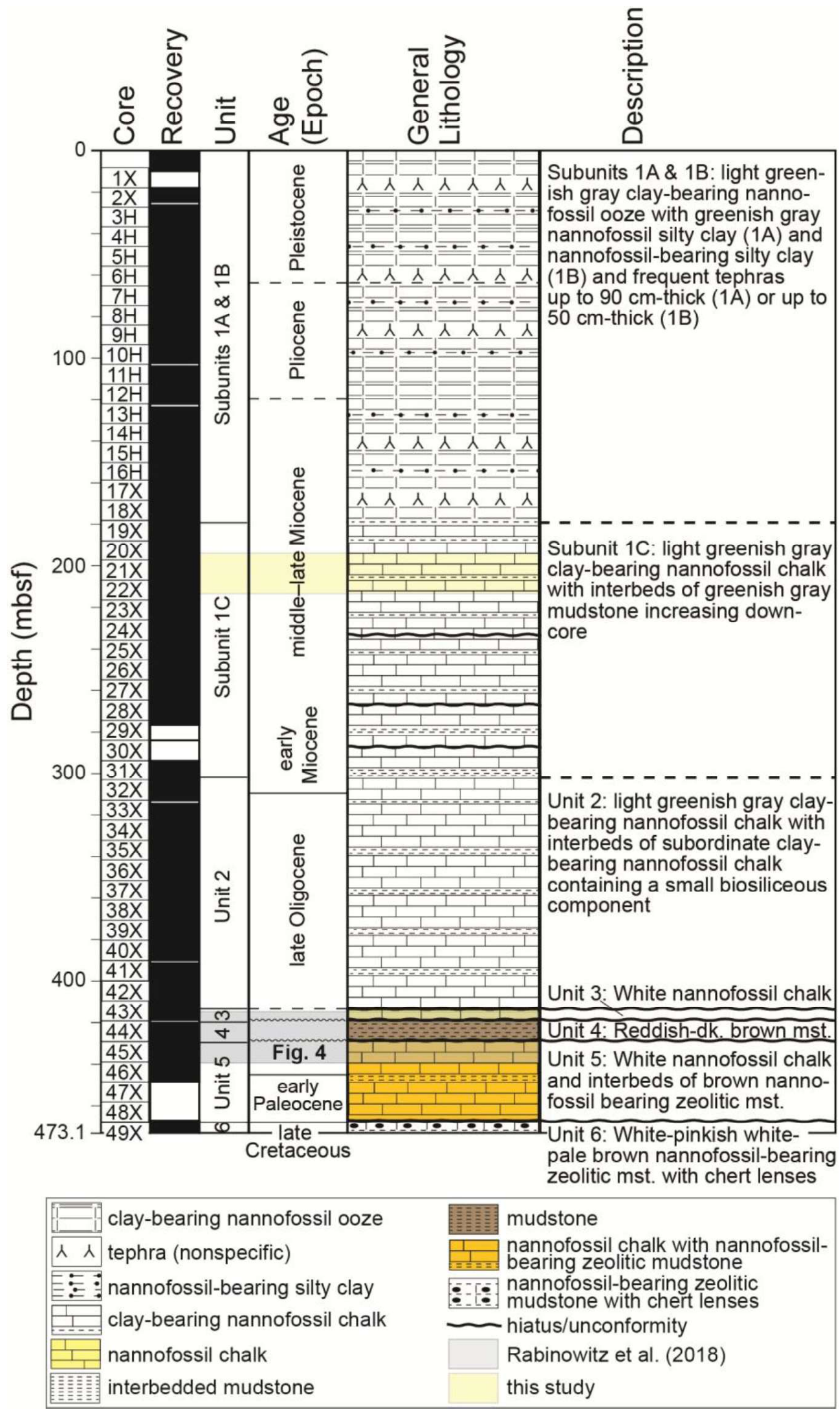

Figure 2. Summary of ODP Site 1124, Hole 1124C stratigraphy. Lithological units and descriptions were determined shipboard during ODP Leg 181 and reported in Carter et al. (1999). This study focuses on Units 3, 4, and 5 between 419.1 mbsf and 445.54 mbsf, an interval that spans the early Oligocene to middle Paleocene. Previous research by Rabinowitz et al. (2018) measured the mineralogical and frictional properties of a Subunit 1C (Miocene) clay-bearing nannofossil chalk sample composed of material recovered from between 194 mbsf and 213.48 mbsf (figure after Carter et al., 1999).

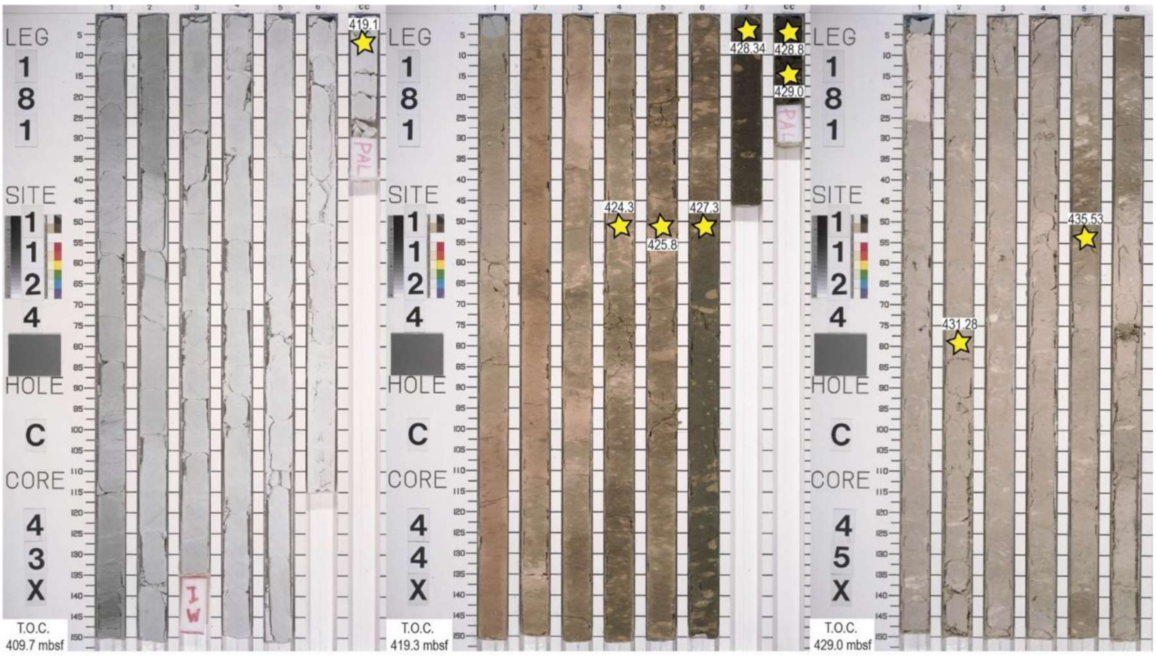

Figure 3. Early Oligocene (181-1124C-43X), middle-upper Eocene to mid-Paleocene (181-1124C-44X), and mid-Paleocene (181-1124C-45X) sediments recovered at Site 1124 (39°29.9014‘S, 176°31.8938‘W). Sediments sampled for X-ray diffraction, biostratigraphy, and frictional properties experiments are starred, and the top of the sampled interval is given above the star in meters below sea floor (mbsf). T.O.C. denotes top of core in mbsf. Edited photographs downloaded from http://iodp.tamu.edu/janusweb/imaging/photo.cgi.

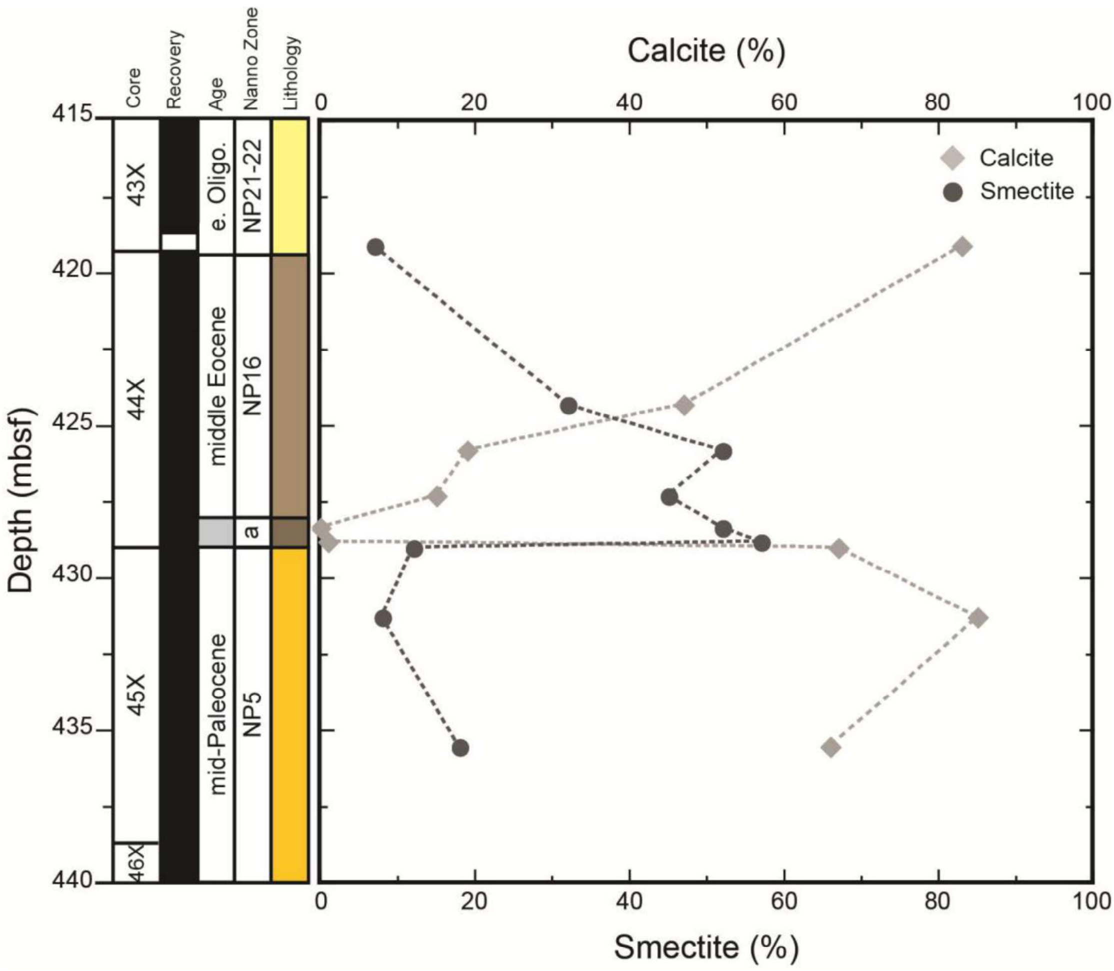

Figure 4. Summary of quantitative XRD and biostratigraphy results. Diagnostic bioevents were correlated with an age using GTS 2012 (Gradstein et al., 2012). Results show a condensed Eocene sequence containing up to 57% (± 2%) smectite (circles) bounded by older and younger chalks containing 66–83% (± 0.5%) calcite (diamonds). Nannofossil zone is abbreviated Nanno Zone; within this column, a is mixed NP5 and NP16.

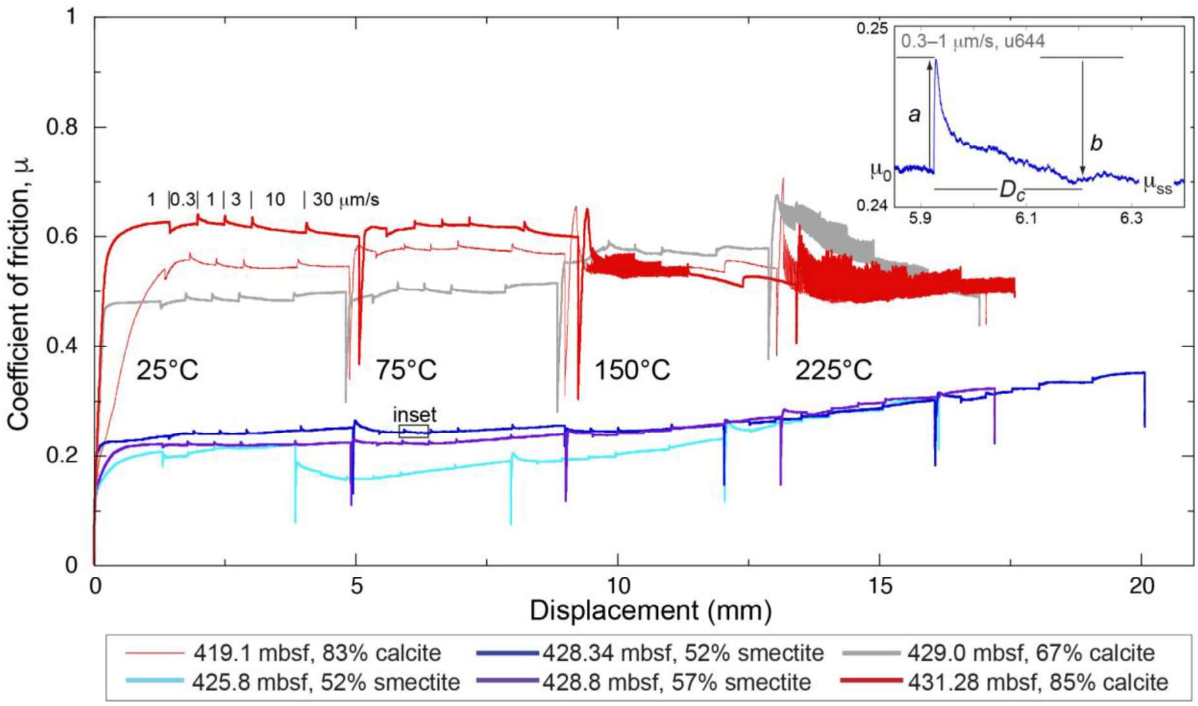

Figure 5. A plot of coefficient of friction ($\mu=\tau/\sigma_n$') vs. displacement showing that mineralogy correlates with strength; chalks containing the most calcite (419.1 and 431.28 mbsf) are the strongest, and clays (425.8, 428.34, and 428.8 mbsf) are the weakest. Inset figure depicts the rate and state friction parameters. All experiments were performed at 60 MPa effective normal stress.

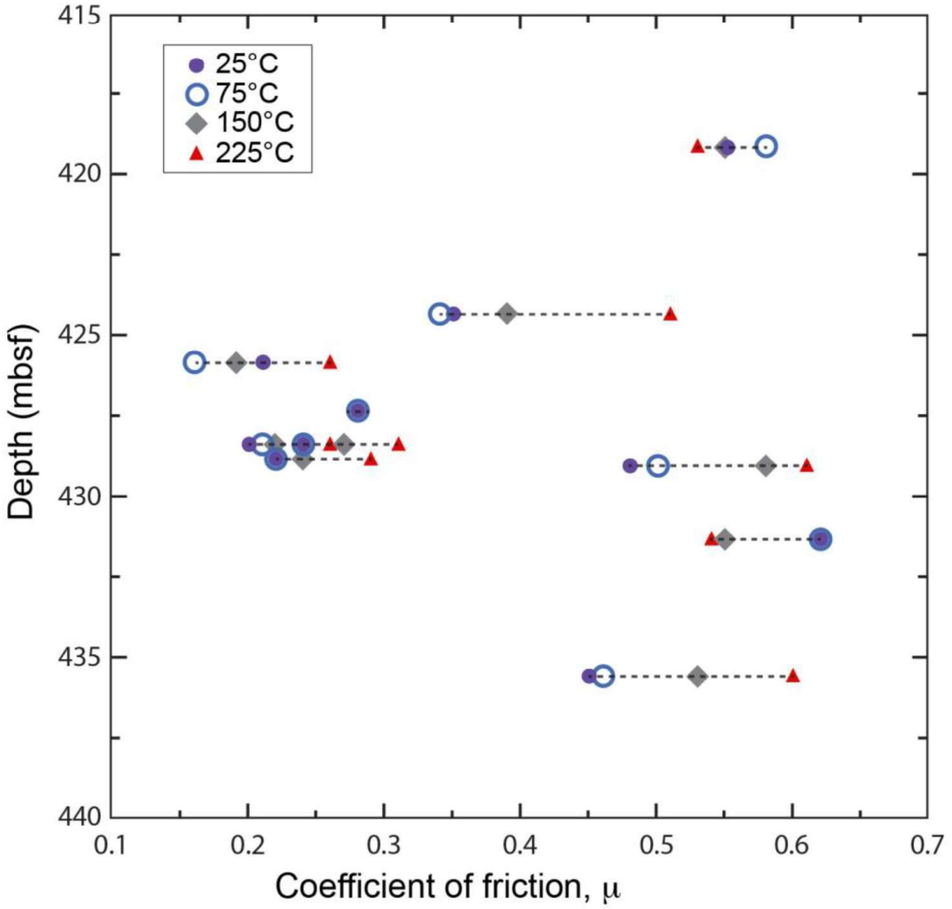

Figure 6. Borehole depth in meters below sea floor (mbsf) vs. coefficient of friction results. The friction coefficient, μ, is calculated as shear stress/effective normal stress ignoring cohesion. Friction coefficients are color and symbol coded for different temperatures, 25°C (blue circles), 75°C (green open circles), 150°C (grey diamonds), and 225°C (red triangles). Experiments were performed at a constant effective normal stress of 60 MPa. Dashed lines connect results from the same sample. Results can be readily compared to borehole depth vs. mineralogy data plotted in Figure 4, noting the inverse correlation between percent smectite (montmorillonite) and friction coefficient at all temperatures tested. Repeat experiments (u644 and u713) on sample 181-1124C-44X-7, 4-6 cm (428.34 mbsf), yielded an analytical error of 0.03-0.05 μ. The analytical error is thought to reflect the fact that the second experiment was performed on the last remaining sample powder, which may have had more fine-grained clays (e.g., sample inter-variability), and/or because of variations in sample preparation.

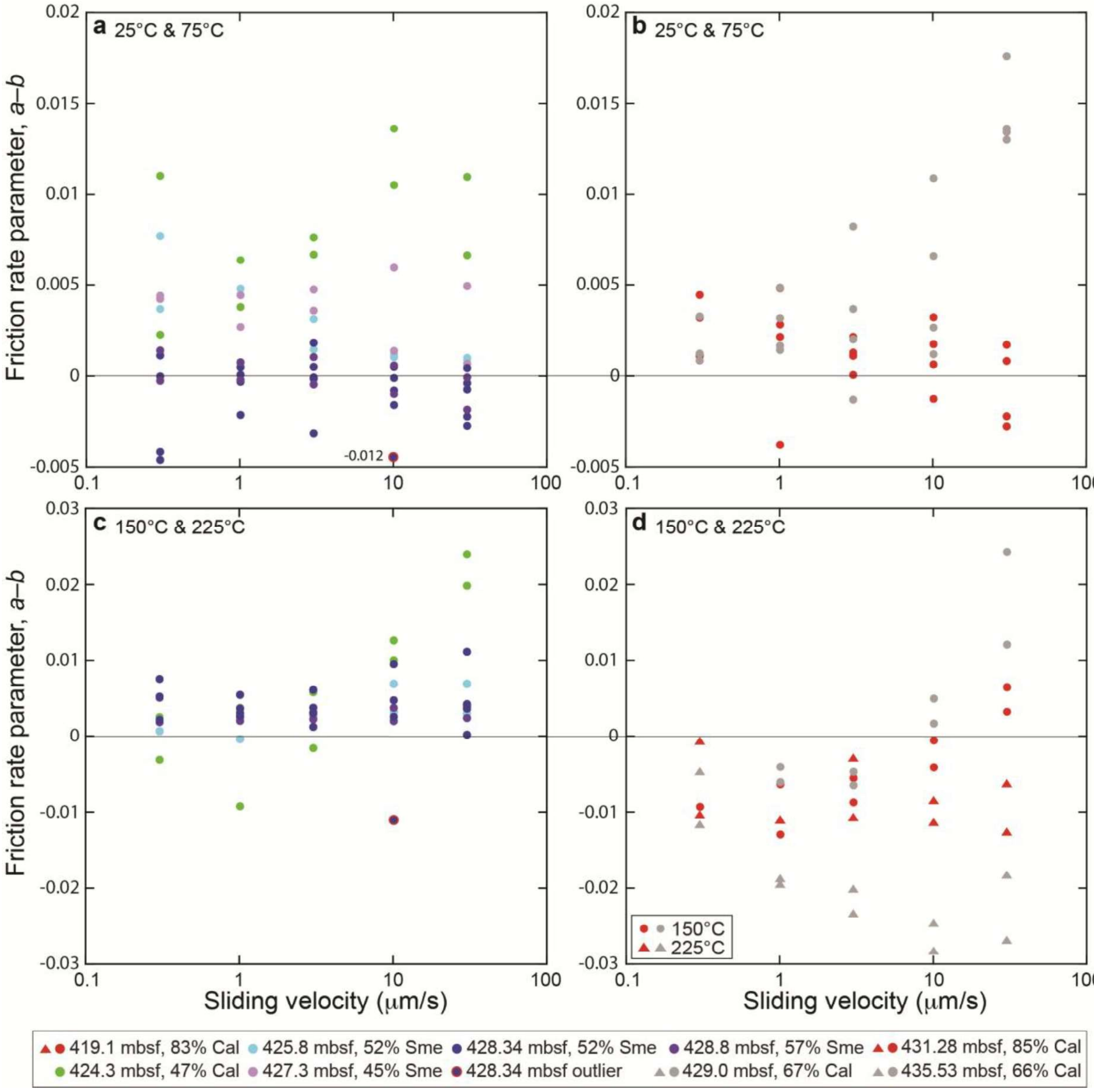

Figure 7. Hydrothermal friction experiments results showing the frictional stability of chalks and clays at temperatures of 25°C, 75°C, 150°C and 225°C. (**a**) Friction rate parameter (*a–b*) results for a clayey ooze (424.3 mbsf) and clays (425.8, 428.34, and 428.8 mbsf) at *T*=25°C and 75°C. Increasing smectite content correlates with decreasing frictional stability. (**b**) Results for chalks (419.1, 429.0, 431.28, and 435.53 mbsf) at *T*=25°C and 75°C. (**c**) Results for a clayey ooze and clays at *T*=150°C and 225°C. There are no data for clay 427.3 mbsf because the furnace failed. (**d**) Results for chalks at *T*=150°C (circles) and 225°C (triangles). At *T*=225°C, chalks exhibit rate-weakening behaviour and stick-slip instabilities at all velocities tested.

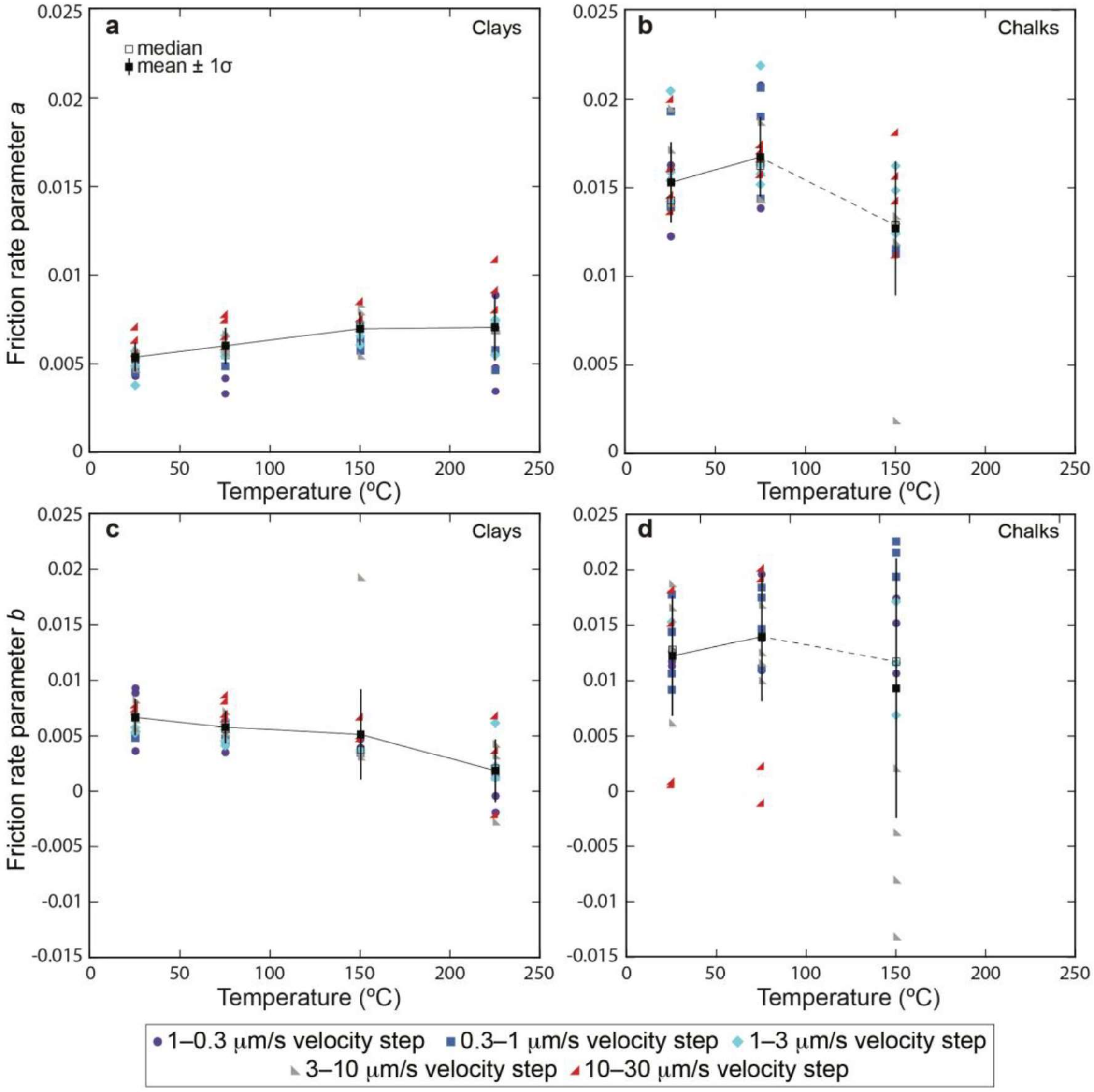

Figure 8. Temperature-dependent changes in *a* and *b* during experiments performed on Hole 1124C clays (52-57% montmorillonite; experiments u644, u713, u639) **(a, c)** and Hole 1124C chalks (66-85% calcite; experiments u643, u645, u657, and u656) **(b, d)**. For the clay samples, as temperature increases from 25°C to 225°C, **(a)** *a* exhibits small increases in median and mean values and **(b)** *b* decreases. As temperature increases from 25°C to 150°C in the chalk samples, **(b)** *a* and **(d)** *b* exhibit no systematic trend. As shown in the legend, symbols are coded by shape and colour to indicate sliding velocities during the velocity step. Where outliers are present, the trend is shown by a dashed line. Solid lines are drawn between mean values. Complete temperature- and velocity-dependent results for the individual rate parameters and critical slip distances are plotted in Appendix Figures A.4, A.5, A.6, and A.7.

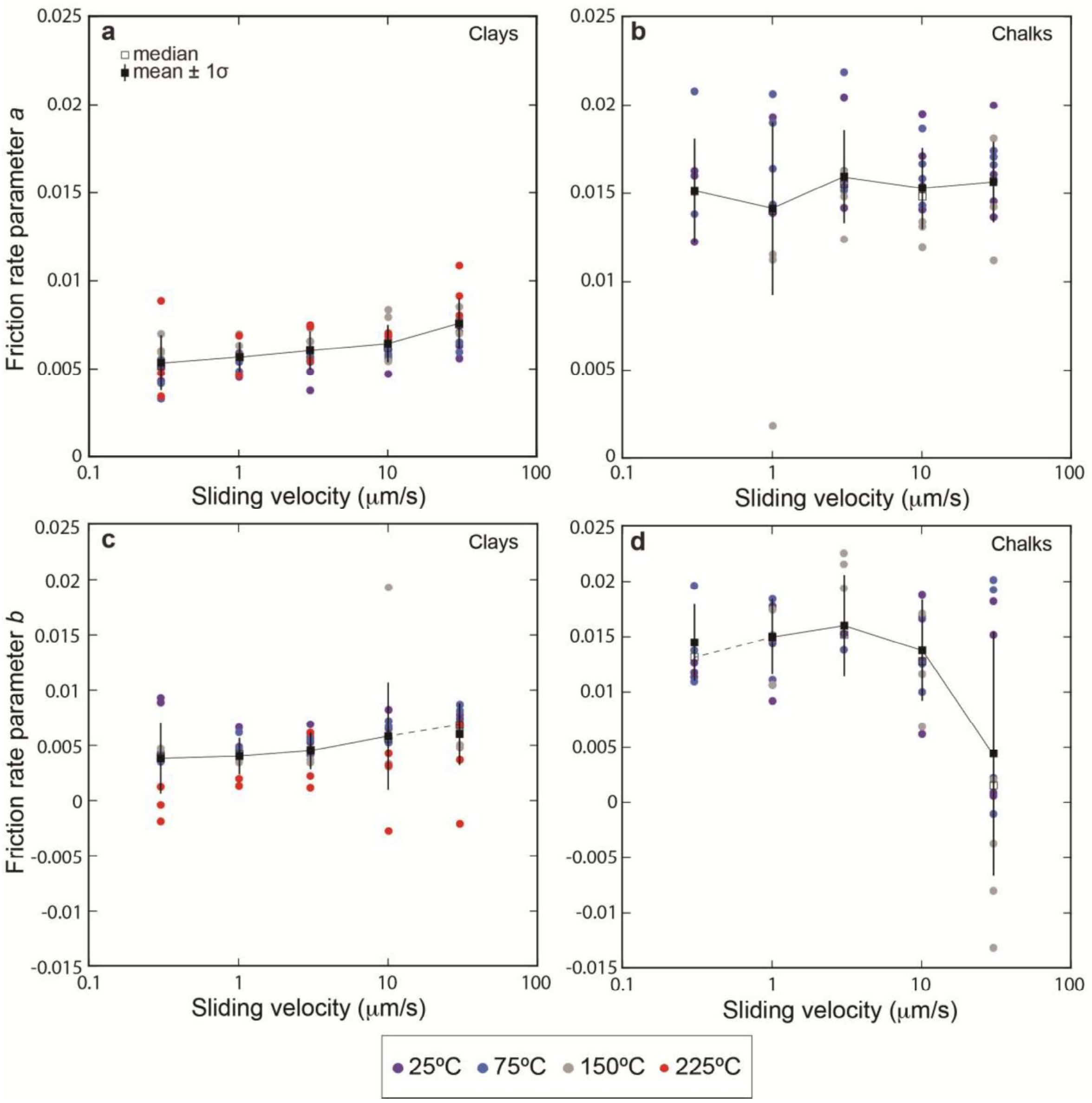

Figure 9. Velocity-dependent changes in *a* and *b* during experiments performed on Hole 1124C clays (52-57% montmorillonite; experiments u644, u713, u639) **(a, c)** and Hole 1124C chalks (66-85% calcite; experiments u643, u645, u657, and u656) **(b, d)**. In the clay samples, as sliding velocity increases from 0.3 to 30 μm/s, **(a)** *a* increases, and **(c)** *b* increases as sliding velocity increases from 1 to 30 μm/s. In the chalk samples, no correlation exists between sliding velocity and **(b)** *a* or **(d)** *b*. As seen in the legend, symbols are colour coded by temperature. Dashed lines indicate the trend where outliers are present. Solid lines are drawn between mean values.

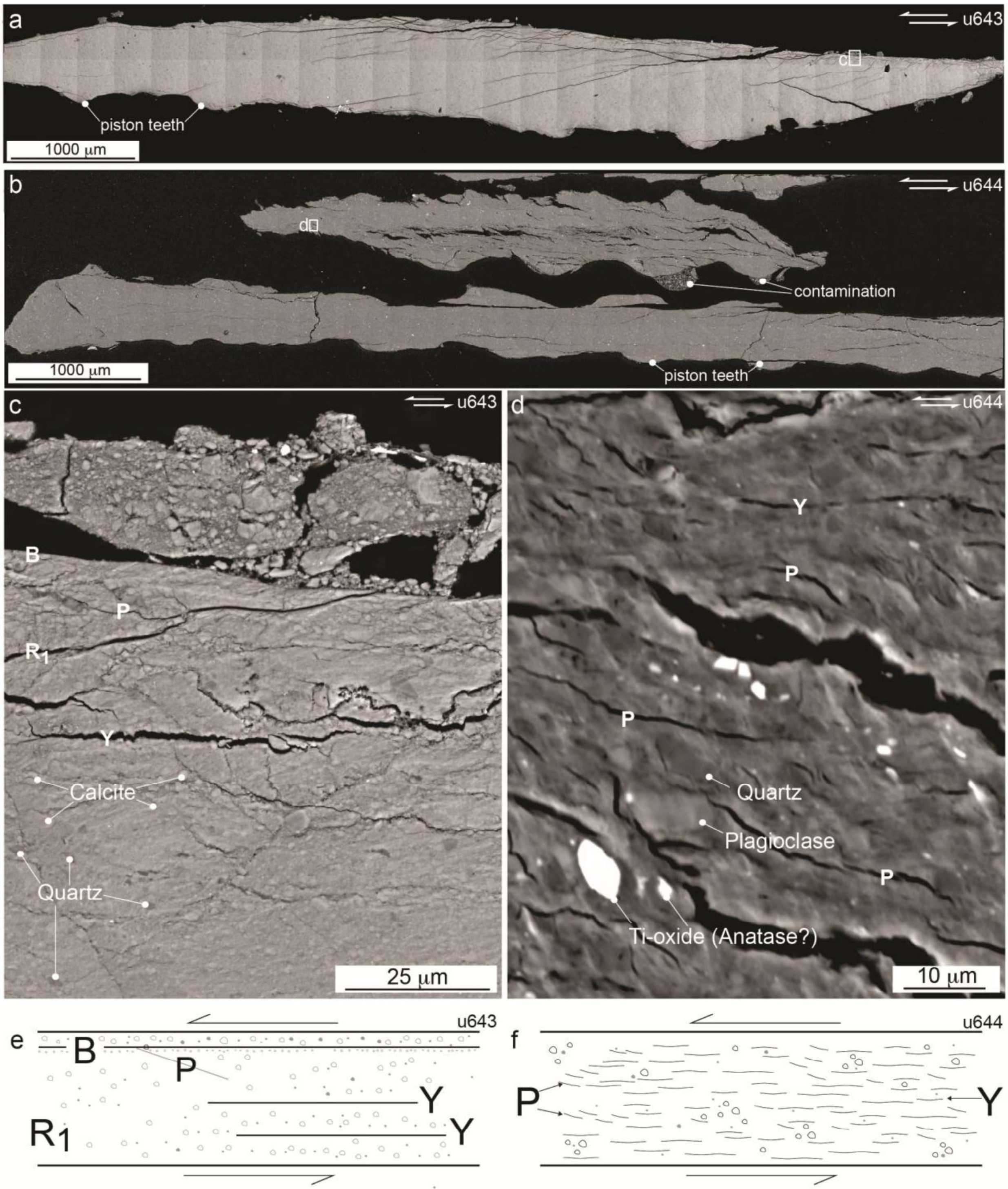

Figure 10. Microstructural analysis was performed on sheared samples recovered from experiment u643 on sample 181-1124C-43X-CC, a clay-bearing nannofossil chalk (chalk) comprising 83% calcite and sample 181-1124C-44X-7, 4-6, a clay comprising 53% smectite (montmorillonite). **(a)** A low magnification scanning electron microscopy backscattered electron (SEM BSE) composite image of chalk showing several localized shears, along which open fractures formed upon unloading. **(b)** Scanning electron microscopy backscattered electron (SEM BSE) images of sheared clay showing several open cracks, which formed along clay-rich surfaces during unloading and drying. The cracks are interpreted to form predominantly along a network of discontinuous Y and P shears. **(c)** Higher magnification

image of the chalk showing grain size reduction within the boundary (B) shear as well as the subordinate P, R_1, and Y localization structures. Quartz appears as dark grey grains (closed white circles), and calcite is light grey (closed white circles). Location of figure (c) given by white rectangle in figure (a). **(d)** Higher magnification image of the clay showing cracks formed within the extremely fine-grained clay matrix during drying. The dominant set is oriented subparallel to the shear zone boundaries (Y-shears) and fine, discontinuous cracks (P-shears) are oblique to the shear zone boundaries. Larger ($\leq$10 μm) grains of titanium oxide, plagioclase, and quartz are identified (closed white circles). While titanium oxide was not identified in XRD, it occurs conspicuously as bright grains within the clay sediments. Location of figure (d) given by white rectangle in figure (b). **(e)** Interpretation of microstructures developed in the chalk. **(f)** Interpretation of microstructures developed in the clay.

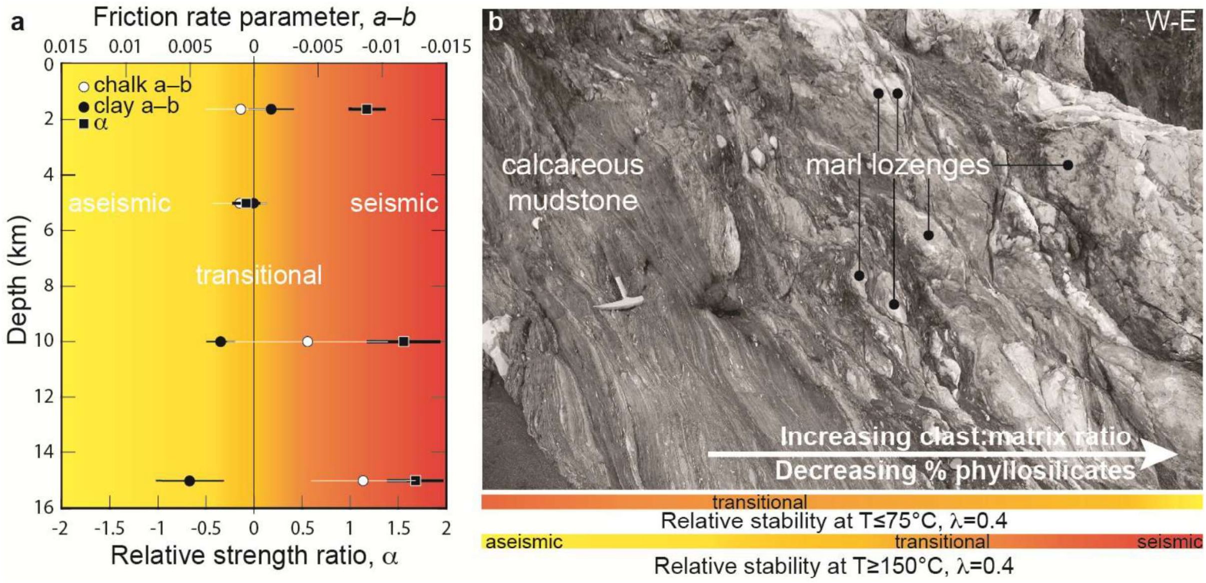

Figure 11. In heterogeneous fault zones, the seismic-to-aseismic transition may be governed by both the (a) relative strength ratio (α) and the (b) distribution of rate-strengthening to rate-weakening material (see text for a full discussion). **(a)** Relative strength ratios (α) (black squares with white rim) were calculated from mean (*a–b*) values measured from velocity steps between 0.3 and 30 μm/s performed on Site 1124 clays containing 52–57% montmorillonite (experiments u644, u713, and u639; black circles) and Site 1124 chalks containing 83–85% calcite (experiments u643 and u657; white circles with black rim). Error bars on clay and chalk (*a–b*) values are standard deviations (±1σ) and reflect primarily the velocity dependence of (*a–b*), as well as analytical error and inter-sample variability. Error bars on (α) were calculated from standard deviations in (*a–b*) using standard error propagation methods. Temperature is converted to depth assuming a geothermal gradient of 15°C/km; note experiments were performed at σ_n'= 60 MPa with hydrostatically pressured pore fluids. The relative strength ratio approaches zero when pore fluid pressure approaches lithostatic values in both the rate-strengthening and rate-weakening sediments (vertical line at X=0); seismic behaviour is promoted when pore-fluid overpressures develop in rate-weakening sediments. **(b)** Along a fault, slip mode correlates with lithology and the relative proportion of contrasting lithologies. The Hungaroa Fault Zone, Tora, contains a ~40 m-wide tectonic mélange formed within Eocene calcareous clays and marls of the Wanstead Formation. Given the ubiquitous presence of detrital montmorillonite in the sediments, deformation is interpreted to have taken place at temperatures <100–150°C. The calcareous mudstones generally contain less montmorillonite (17–35%) than those recovered from Site 1124, but fabrics developed within the sequence are interpreted to be representative of those that would form in a décollement composed of clays and chalks. The qualitative scale bars indicate that predominantly transitional behaviour is anticipated for clays, chalks, and chalk-clay mixtures at *T*≤75°C. At *T*≥150°C, a higher proportion rate-weakening marls promotes seismic behaviour.

Table 1

Table 1. *Summary of hydrothermal friction experiment and X-ray diffraction results*

Exp.	Depth (mbsf)[a]	ODP sample[b]	Cal, Sme, Zeo (%)[c]	T (°C)[d]	μ[e]	(a–b)[f]
u643	419.1	181-1124C-43X-CC	83, 7, 4	25, 75, 150, 225	0.55, 0.58, 0.55, 0.53	–0.004, 0.002, –0.006, –0.01
u647	424.3	181-1124C-44X-4, 50-53	47, 32, 12	25, 75, 150, 225	0.35, 0.34, 0.39, 0.51	0.006, 0.004, 0.004, 0.003
u638	425.8	181-1124C-44X-5, 50-53	19, 52, 12	25, 75, 150, 225	0.21, 0.16, 0.19, 0.26	0.005, 0.0006, 0.003, –0.0003
u648	427.3	181-1124C-44X-6, 50-53	15, 45, 24	25, 75	0.28, 0.28	0.004, 0.003
u644	428.34	181-1124C-44X-7, 4-6	0, 52, 20	25, 75, 150, 225	0.24, 0.24, 0.27, 0.31	0.0005, –0.0003, 0.003, 0.005
u713	428.34	181-1124C-44X-7, 4-6	0, 52, 20	25, 75, 150, 225	0.20, 0.21, 0.22, 0.26	–0.002, 0.0001, 0.003, 0.004
u639	428.8[g]	181-1124C-44X-CC (dark)	<1, 57, 17	25, 75, 150, 225	0.22, 0.22, 0.24, 0.29	–0.0002, 0.0008, 0.002, 0.003
u645	429[g]	181-1124C-44X-CC (light)	67, 12, 13	25, 75, 150, 225	0.48, 0.50, 0.58, 0.61	0.003, 0.001, –0.004, –0.02
u657	431.28	181-1124C-45X-2, 78-82	85, 8, 4	25, 75, 150, 225	0.62, 0.62, 0.55, 0.54	0.005, 0.003, –0.01, –0.01
u656	435.53	181-1124C-45X-5, 53-56	66, 18, 9	25, 75, 150, 225	0.45, 0.46, 0.53, 0.60	0.005, 0.002, –0.006, –0.02

[a]mbsf=meters below sea floor at top of sampled interval. [b]Samples named following standard procedure, where 181-1124C-44X-5, 50-53 is Expedition 181-Hole 1124C-Core 44X-Section 7, 50-53 cm below top of section. X denotes extended core barrel. [c]Abbreviations are calcite (Cal), smectite (Sme), and zeolite (Zeo). Unit is modal %. [d]Temperature was increased following each set of velocity steps. [e]Friction coefficient, μ, taken as shear stress/effective normal stress at 1 μm/s sliding velocity for each temperature tested. [f]Representative friction rate parameter (*a–b*) measured from the 0.3-1 μm/s velocity step at each temperature tested. [g]Samples obtained from the core catcher (CC), 428.75 mbsf to 429.0 mbsf; depths assigned based on colour variations in core photos with ± 0.25 mbsf uncertainty. All experiments performed at 60 MPa effective normal stress with hydrostatic pore pressure controlled manually.

Editable Table 1

Click here to download Table: Boulton_etal_1124_Table1_Final.xlsx

Table 1. *Summary of hydrothermal friction experiment and X-ray diffraction results*

Exp.	Depth (mbsf)[a]	ODP sample[b]	Cal, Sme, Zeo (%)[c]	T (°C)[d]	μ[e]	(a–b)[f]
u643	419.1	181-1124C-43X-CC	83, 7, 4	25, 75, 150, 225	0.55, 0.58, 0.55, 0.53	–0.004, 0.002, –0.006, –0.01
u647	424.3	181-1124C-44X-4, 50-53	47, 32, 12	25, 75, 150, 225	0.35, 0.34, 0.39, 0.51	0.006, 0.004, 0.004, 0.003
u638	425.8	181-1124C-44X-5, 50-53	19, 52, 12	25, 75, 150, 225	0.21, 0.16, 0.19, 0.26	0.005, 0.0006, 0.003, –0.0003
u648	427.3	181-1124C-44X-6, 50-53	15, 45, 24	25, 75	0.28, 0.28	0.004, 0.003
u644	428.34	181-1124C-44X-7, 4-6	0, 52, 20	25, 75, 150, 225	0.24, 0.24, 0.27, 0.31	0.0005, –0.0003, 0.003, 0.005
u713	428.34	181-1124C-44X-7, 4-6	0, 52, 20	25, 75, 150, 225	0.20, 0.21, 0.22, 0.26	–0.002, 0.0001, 0.003, 0.004
u639	428.8[g]	181-1124C-44X-CC (dark)	<1, 57, 17	25, 75, 150, 225	0.22, 0.22, 0.24, 0.29	–0.0002, 0.0008, 0.002, 0.003
u645	429[g]	181-1124C-44X-CC (light)	67, 12, 13	25, 75, 150, 225	0.48, 0.50, 0.58, 0.61	0.003, 0.001, –0.004, –0.02
u657	431.28	181-1124C-45X-2, 78-82	85, 8, 4	25, 75, 150, 225	0.62, 0.62, 0.55, 0.54	0.005, 0.003, –0.01, –0.01
u656	435.53	181-1124C-45X-5, 53-56	66, 18, 9	25, 75, 150, 225	0.45, 0.46, 0.53, 0.60	0.005, 0.002, –0.006, –0.02

[a]mbsf=meters below sea floor at top of sampled interval. [b]Samples named following standard procedure, where 181-1124C-44X-5, 50-53 is Expedition 181-Hole 1124C-Core 44X-Section 7, 50-53 cm below top of section. X denotes extended core barrel. [c]Abbreviations are calcite (Cal), smectite (Sme), and zeolite (Zeo). Unit is modal %. [d]Temperature was increased following each set of velocity steps. [e]Friction coefficient, μ, taken as shear stress/effective normal stress at 1 μm/s sliding velocity for each temperature tested. [f]Representative friction rate parameter (*a–b*) measured from the 0.3-1 μm/s velocity step at each temperature tested. [g]Samples obtained from the core catcher (CC), 428.75 mbsf to 429.0 mbsf; depths assigned based on colour variations in core photos with ± 0.25 mbsf uncertainty. All experiments performed at 60 MPa effective normal stress with